A nested grid model of the Oregon Coastal Transition Zone: Simulations and comparisons with observations during the 2001 upwelling season

S. R. Springer,[1,2] R. M. Samelson,[1] J. S. Allen,[1] G. D. Egbert,[1] A. L. Kurapov,[1] R. N. Miller,[1] and J. C. Kindle[3]

[1] The Oregon Coastal Transition Zone (OCTZ) extends several hundred kilometers offshore where shelf flows interact with the northern California Current. A primitive-equation numerical ocean model is used to study the upwelling circulation in this region from 1 May to 1 November 2001. This OCTZ model obtains initial and boundary conditions from a larger-scale model of the California Current System and forcing from a regional atmospheric model product. The model results are compared with extensive in situ and remotely sensed data, and the model is found to provide a realistic representation of flows both over the shelf and in the broader OCTZ. Simulation of coastal sea level and shelf currents over the complex topography of the central Oregon coast is improved quantitatively relative to previous regional models. A particularly significant qualitative improvement is realistic representation of coastal jet separation and eddy formation offshore of Cape Blanco. Three-dimensional Lagrangian analysis of water parcel displacement shows that the surface waters inshore of the separated jet are upwelled from near the bottom along the shelf as far north as 45.5°N. A large eddy, which incorporates some of this upwelled water and carries it farther westward, forms offshore in the late summer. Ensemble simulations show a distinction between the strongly deterministic response to wind forcing over the shelf and the more unstable, less predictable jet separation and offshore eddy formation processes in the region near Cape Blanco.

1. Introduction

[2] Near the eastern boundary of the north Pacific Ocean, the southward flow of the California Current is influenced by coastal circulation. Beginning in early spring and lasting until late fall, predominantly southward wind stress forces coastal upwelling, which contributes to the formation of a narrow, surface-intensified southward jet [*Huyer*, 1983]. Water properties differ on either side of the jet, with relatively colder, saltier, more nutrient rich, and more biologically productive waters on the shoreward side. During the summer and early fall the jet separates from the coastline near Cape Blanco (42.8°N), a major headland on the Oregon coast [*Barth et al.*, 2000]. South of that location the separated current forms jets, plumes, and eddies in an area that extends hundreds of

kilometers offshore [*Strub and James*, 2000]. This area over which mesoscale and submesoscale features mix the distinctive shelf and slope waters with those of the open ocean is known as the coastal transition zone [*Brink and Cowles*, 1991]. Here we focus on the Oregon Coastal Transition Zone (OCTZ), which extends from the north side of Cape Mendocino, California (40.5°N), to north of Cape Elizabeth, Washington (47.3°N), and approximately 400 km offshore.

[3] The complexity of flow in the OCTZ indicates that a numerical modeling approach will be valuable in understanding the dynamical processes involved and the pathways taken by water parcels from shelf to open ocean. Because of disparate time and space scales of the shelf and open ocean, past modeling studies have tended to focus on one or the other, neglecting interaction between the two. Modeling studies of the central Oregon shelf [*Oke et al.*, 2002a, 2002b; *Kurapov et al.*, 2005a, 2005b, 2005c; *Gan and Allen*, 2005a; *Gan et al.*, 2005] have used high horizontal (1−2 km) and vertical resolution (up to 60 sigma levels) to represent topographic influences and boundary layer structure. Forced by winds with daily temporal resolution, such models realistically simulate flows on the inner and midshelf for periods of 50−100 days, but none develops separation of the coastal

[1]College of Oceanic and Atmospheric Sciences, Oregon State University, Corvallis, Oregon, USA.
[2]Earth and Space Research, Seattle, Washington, USA.
[3]Oceanography Division, Naval Research Laboratory, Stennis Space Center, Mississippi, USA.
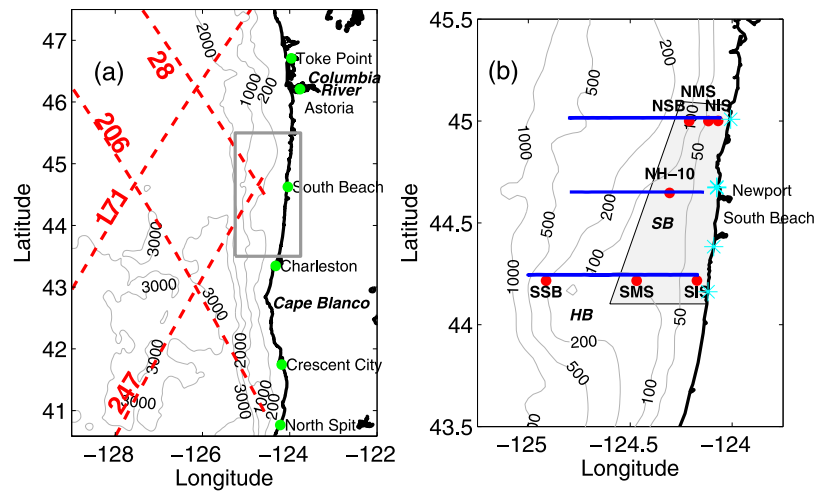
Figure 1. (a) The entire model domain with contours of the smoothed bottom topography in meters used in the model. Green dots along the coast show the positions of tide gauges together with their names. Dashed red lines are the ground tracks of the TOPEX/Poseidon satellite with their identifiers. (b) A close-up of the area enclosed by the gray box in Figure 1a showing details in the vicinity of Heceta Bank (indicated by HB) and Stonewall Bank (indicated by SB). Moorings are indicated by red dots. The blue lines are the portions of the high-resolution hydrographic survey used here. Light blue asterisks are the positions of the HF radar stations, which measure surface currents over the approximate region in the shaded area.

jet at Cape Blanco, mesoscale eddies, or realistic flow in the offshore region. On the other hand, these features of the large-scale circulation have been simulated in models of the California Current System (CCS) [e.g., *Batteen*, 1997; *Shulman et al.*, 2004], but the horizontal (typically 9–10 km) and vertical grid resolutions and temporal resolution of the forcing are inadequate to simulate details of the circulation on the narrow (10–50 km) Oregon shelf. In the cases where the entire CCS is modeled at sufficiently high spatial resolution [*Marchesiello et al.*, 2003; *Powell et al.*, 2006], little attention has been paid to comparing the shelf circulation with observations.

[4] In this study, a one-way, nested grid model is developed to study the interaction of shelf flows with the CCS in the OCTZ. The spatial resolution is sufficient to represent the shelf circulation, and the effects of the large-scale circulation are imposed through boundary and initial conditions. The primary objective is to develop a model which represents these flows better than either the previous regional OCTZ or larger-scale CCS models. Validation of the nested model is carried out by quantitative comparison with data from existing elements of the Oregon coastal ocean observing system and major field programs. Similar comparisons are done using the outer model simulation to demonstrate whether and how the nested model improves on its solutions. Comparisons with previous regional models by reference to existing work helps establish what factors contribute to the improvement of simulations in the nested model and identify a physical mechanism. A second objective is to examine disturbance growth of these flows and identify the role of initial conditions in error growth. The ultimate objective of having a realistic model is to gain physical insight into phenomena such as the separation of the coastal jet at Cape Blanco during upwelling. A preliminary investigation using tracers shows the intimate con-

nection between upwelling shelf flows and the separated currents.

2. Model and Data

2.1. Model Description

[5] The OCTZ model is based on the Regional Ocean Modeling System (ROMS version 2.2) [*Shchepetkin and McWilliams*, 2005; *Haidvogel et al.*, 2008], a discretization of the hydrostatic primitive equations with a free surface. A parabolic splines density Jacobian scheme is used for pressure gradient calculations [*Shchepetkin and McWilliams*, 2003], and a third-order, upwind-biased scheme is used in horizontal momentum and tracer advection. A fourth-order, centered scheme is used for vertical advection of tracers. Subgridscale mixing is parameterized by the Mellor-Yamada Level 2.5 model in the vertical direction [*Mellor and Yamada*, 1982; *Wijesekera et al.*, 2003], and by harmonic diffusivity and viscosity, both with coefficients of 20 m²/s, in the horizontal direction. Lateral diffusion of tracers is restricted to isopycnals to minimize problems related to the interaction of strong horizontal mixing and steep bottom topography [*Dinniman and Klinck*, 2002].

[6] The domain extends from 40.6°N to 47.5°N and from 123.7°W to 129°W, approximately 400 km offshore (Figure 1a). The 136×250 point horizontal grid is specified in spherical polar coordinates with a uniform resolution of $5/128°$ in longitude and $1/36°$ in latitude, giving approximately 3.1 km resolution within the domain. The Coriolis parameter varies with latitude. The vertical grid has 40 levels of terrain-following coordinate with enhanced resolution near the lower and upper boundaries specified by the stretching parameters $q_b = 0.2$ and $q_s = 6.0$ [*Song and Haidvogel*, 1994]. Bottom topography is a bilinear interpolation of ETOPO5 gridded data [*NGDC*, 1988] in deep waters offshore blended with high-resolution data that better represent details of the
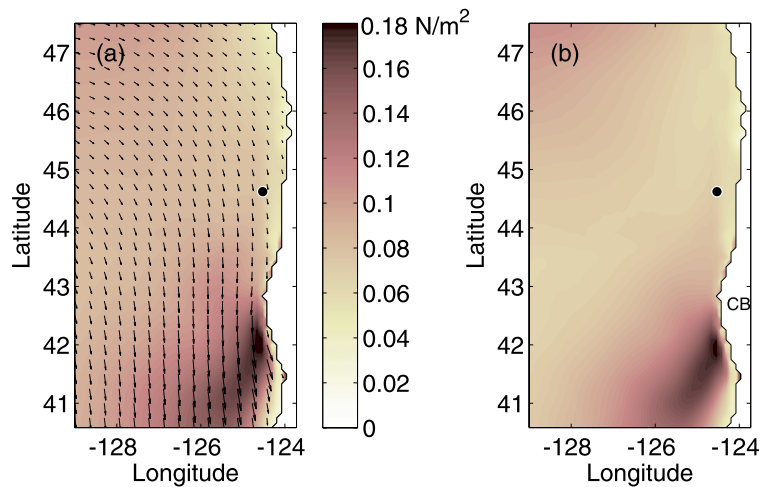
Figure 2. (a) Mean and (b) standard deviation of wind stress over days 121–305. Vectors show mean wind stress. Black dot indicates position of NOAA buoy 46050. Cape Blanco is designated CB.

slope and shelf. Minimum water depth along the coast is fixed at 20 m, but no limitation on maximum depth is imposed. Bottom slopes are smoothed to meet the r-factor criterion of 0.2, which reduces pressure gradient errors in terrain-following coordinates [*Beckmann and Haidvogel*, 1993].

2.2. Initial and Boundary Conditions

[7] The coastline, which is represented as discrete stair steps, forms a closed eastern boundary where there is no normal flow and a free slip condition applies to tangential flow. The northern, southern, and western edges are open boundaries. We use a *Chapman* [1985] condition on the free surface and a *Flather* [1976] condition on depth-averaged velocities normal to the open boundaries. The boundary condition applied to three-dimensional velocities and tracers is based on the radiation and nudging scheme described by *Gan and Allen* [2005b] with a modification for oblique radiation [*Marchesiello et al.*, 2001]. The nudging time scale is 100 days on outflow and 1 day on inflow. In a sponge layer at the open western and southern (but not northern) boundaries, the diffusivity and viscosity coefficients are set equal to $100 \text{ m}^2/\text{s}$ at the boundaries and tapered over 150 km to their interior values. This nesting strategy was selected as the best after a series of experiments which are not detailed here.

[8] Data for initial and boundary conditions are derived from Navy Coastal Ocean Model (NCOM) [*Shulman et al.*, 2004]. The California Current System (CCS) domain extends from 30°N to 49°N and from 115°W to 135°W in spherical coordinates at 1/12° (9–10 km) horizontal resolution. The vertical coordinate is a hybrid with σ levels at water depths of less than 138 m, giving high resolution on the shelf, and z levels at greater depths. The version of NCOM-CCS used here did not assimilate data, but it was itself one-way nested in a data-assimilating 1/8° global model. Values for variables on the finer OCTZ grid are obtained by interpolation and, where required by differences in the bottom topography, extrapolation in a manner that maintains stable stratification. Boundary data are interpolated linearly in time between twice-daily snapshots. The simulation discussed here in detail is initialized with NCOM-CCS model output from the year 2001 on day 120 (1 May) and run through day 305

(1 November). Additional simulations are initialized from NCOM-CCS fields on days 90, 100, 110, 130, and 140. Since the resulting simulations with ROMS differ slightly on, say, day 141, this procedure tests sensitivity to initial conditions.

2.3. Forcing

[9] Both NCOM-CCS and the OCTZ model are forced with the same wind stress, which was derived from Coupled Ocean/Atmosphere Mesoscale Prediction System (COAMPS) [*Hodur*, 1997], a data-assimilating regional atmospheric model. An Eastern Pacific reanalysis [*Kindle et al.*, 2002] was run on multiply nested grids centered on Monterey Bay, with the boundary between the 9 km and 27 km grids falling just south of 45°N within the OCTZ domain. This simulation reproduces spatial variation of the winds (Figure 2), including the orographically enhanced wind jet to the southwest of Cape Blanco that arises during upwelling-favorable winds [*Samelson et al.*, 2002; *Perlin et al.*, 2004]. Temporal variation of wind stress is highly coherent along the coast. At the location of NOAA weather buoy 46050 (44.62°N 124.53°W; approximately 37 km off Newport, Oregon) the major features of the meridional wind stress time series (Figure 3) are similar to those discussed in detail by *Bane et al.* [2005]. During the period from day 120 to 305 the predominantly (70% of the time) southward, upwelling-favorable nearshore winds were enhanced by approximately a dozen major (southward wind stress exceeding 0.1 N m^{-2}) upwelling-favorable events and reversed by half as many briefer downwelling-favorable (northward wind) events (Figure 3). Zonal wind stress remained relatively small throughout the summer. Hourly COAMPS wind stress is boxcar-averaged to 4-h intervals and is bilinearly interpolated to the OCTZ spatial grid to create forcing for the model.

[10] The COAMPS model provides surface heat fluxes, which were used to force NCOM-CCS. The OCTZ model is also forced by the shortwave radiation component distributed over depth according to the profile associated with Jerlov water type 1 [*Paulson and Simpson*, 1977]. However, initial testing showed that the upper ocean was consistently cool if sensible, latent, and longwave fluxes from COAMPS were
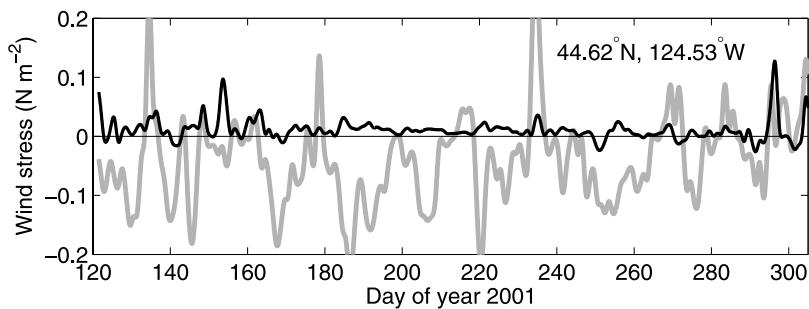
Figure 3. Time series of zonal wind stress (black) and meridional wind stress (gray) sampled from COAMPS model at location closest to NOAA buoy 46050. Prolonged periods of southward, upwelling-favorable winds were interrupted by brief periods of northward, downwelling-favorable winds, or relaxation events.

used to force the OCTZ model; instead, these surface heat fluxes are calculated internally by ROMS using the bulk flux formulation of *Fairall et al.* [1996]. Since the requisite air temperature, humidity, pressure, and cloud cover were not available to us from COAMPS, we use values from NCEP reanalysis [*Kalnay et al.*, 1996]. The coarse (2.5°) grid of the reanalysis product may result in unrealistic values for atmospheric variables and calculated heat fluxes in coastal regions.

[11] No freshwater or salinity flux through the ocean's surface is prescribed. River inflow is neglected, but some influence of freshwater sources enters through the initial and northern boundary conditions. Tidal forcing is not included.

2.4. Data

[12] A variety of data is used for validating the OCTZ model simulations. NOAA tide gauges and TOPEX/Poseidon altimeters provide measurements of sea level (Figure 1a). Tide gauge data are demeaned with the average value for 2001, 40-h low-pass filtered, and corrected for the inverse barometer effect [*Barron et al.*, 2004]. The TOPEX/Poseidon satellite measured sea surface height with a 10-day repeat cycle along four ground tracks, 247, 206, 171, and 28, in the time and region of interest. An absolute dynamic topography product, formed by combining the altimeter-measured anomalies with a mean sea surface topography from a geoid model, in situ density measurements, and multiple years of altimetry data [*Rio and Hernandez*, 2004], is used for the comparisons below. Because this sea level product has a different reference level from NCOM-CCS, a spatially averaged bias of 1.5 m is removed.

[13] As part of Coastal Ocean Advances in Shelf Transport (COAST) [*Barth and Wheeler*, 2005], detailed observations from summer 2001 were made in the region of Stonewall Bank and Heceta Bank, submarine topographic features along the central Oregon shelf extending alongshore from 44.1°N to 45.1°N and offshore to 125°W (Figure 1b). Available data include high-frequency (HF) radar estimates of surface current [*Kosro*, 2005], moored observations of temperature, salinity, and ADCP-measured velocities [*Boyd et al.*, 2002], and high-resolution hydrographic sections [*Barth et al.*, 2005; *Castelao and Barth*, 2005]. Most of the moorings (NIS, NMS, NSB, SIS, SMS, SSB; see Figure 1b) were deployed during days 140–240, but a long-term GLOBEC mooring (NH-10) was in place for the entire time period considered here. In cases in which the model and mooring bottom depth

differ significantly, the model is sampled at a nearby location with a similar bottom depth, rather than the closest possible location. HF radar-measured current velocities are mapped on a 2 km grid, and, for comparisons, the modeled surface velocities are interpolated to the same grid. All mooring and HF radar data and the corresponding model data are smoothed with a 40-h low-pass filter to minimize tidal currents.

3. OCTZ Simulations

3.1. Large-Scale Circulation

[14] The mean model sea surface temperature, salinity, height, and currents over the simulation interval, days 120–305 of year 2001, show a region of cold, saline, low sea surface elevation, and strong, generally southward flow over the shelf and slope (Figure 4). Cold surface temperatures and, especially, high surface salinities are more evident in the southern half of the domain. Some evidence of spurious boundary effects on sea surface temperature and height is suggested in the northwestern part of the domain, but these appear to be limited in amplitude and extent. Persistent offshore flow, extending from the shelf across the slope to the deep interior, occurs near the latitude of Cape Blanco, around 42.8°N (Figure 4d). Offshore extension of the low temperatures, high salinities, and low sea surface heights are also evident at these southern latitudes (Figures 4a–4c). The overall patterns of these mean surface variables are consistent with the coastal upwelling response to the mean upwelling-favorable wind stress during this period (Figure 2). The large cross-shore gradients over the shelf and slope are the mean expression of the coastal upwelling front, separating the cold, saline upwelled water inshore from the warm, fresh surface water offshore, and the large surface currents (up to 0.5 m/s) are the mean expression of the associated geostrophic coastal upwelling jets. Southward intensification of the mean upwelling response is consistent with the southward intensification of the mean wind stress over this region (Figure 2), including the orographic intensification associated with Cape Blanco [*Perlin et al.*, 2004].

[15] A north-south difference in cross-shore location of the surface front, relative to the shelf and slope topography, is evident in zonal cross sections at 41.9°N, 43.21°N, and 44.65°N of the mean model temperature, salinity, and meridional currents (Figure 5). At the two northern sections the upwelling front occurs over the shelf, within the 200 m isobath, but it is farther away from the coast, over deep
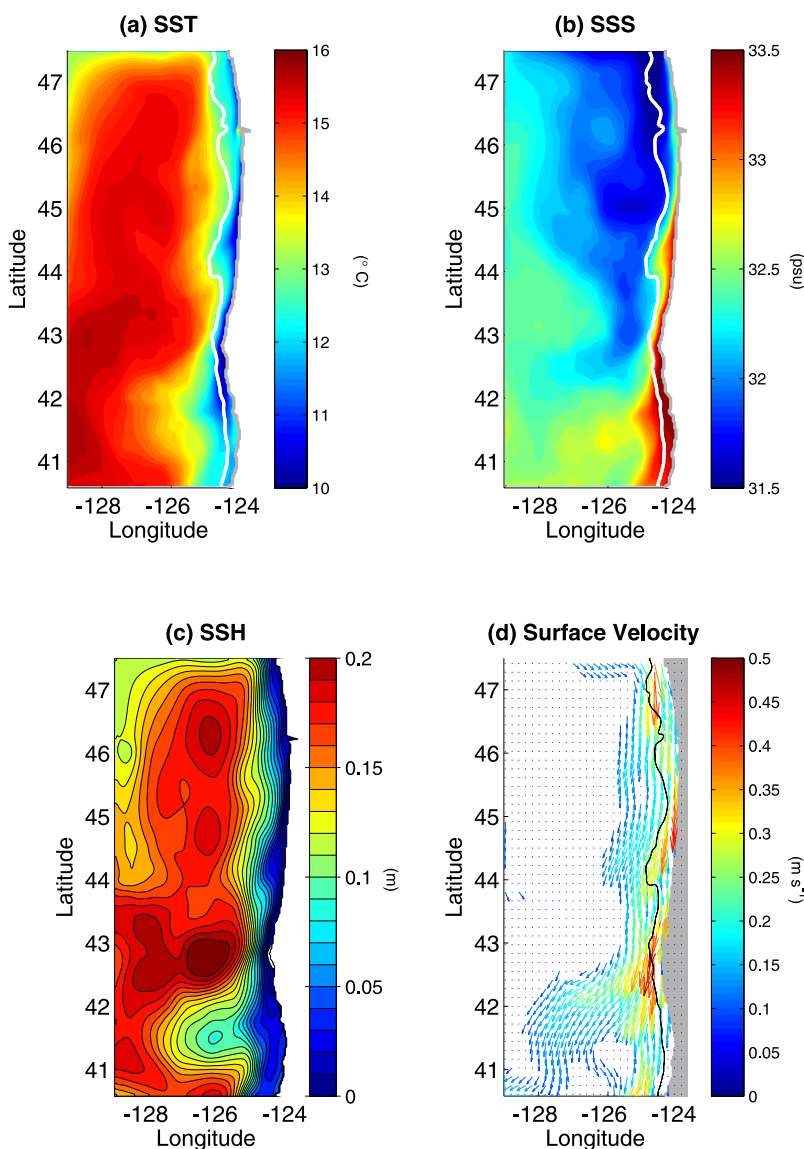
Figure 4. Temporal means (days 121−305) of (a) sea surface temperature (°C), (b) sea surface salinity (psu), (c) sea surface height (m), (d) surface velocity vectors colored by speed (ms^{-1}). Vectors are plotted at every fifth grid point and only where the speed is greater than 0.10 ms^{-1} for clarity.

water, at the southern section. Isohalines and isotherms in the upper ocean slope upward toward the coast, and the geostrophic, southward currents are limited to depths shallower than about 100 m. Beneath about 50−100 m the isotherms and isohalines slope downward onshore, consistent with a northward undercurrent that is found in relatively shallower water, with speed exceeding 0.1 m/s, at the southern section, but is deeper and weaker to the north. As the surface jet moves offshore near Cape Blanco, it crosses over the undercurrent, resulting in a relatively large mean vertical shear near 43.21°N. These features of the undercurrent agree qualitatively with observations [*Pierce et al.*, 2000]. An undercurrent is found in the NCOM-CCS model [*Choboter et al.*, 2006], and it is passed to the OCTZ model through initial and boundary conditions.

[16]　The mean modeled sea surface height can be compared with absolute dynamic topography along several

TOPEX/Poseidon tracks that cross the model domain (Figure 1a) averaged over the simulation time interval (Figure 6). (Note that such a long time average emphasizes the mean part of dynamic topography product rather than the time-dependent anomalies measured by satellite altimetry.) Along the tracks east of 127°W, the time-mean sea surface height drops by 0.1−0.2 m over comparable cross-shore scales in both the observations and the simulation, demonstrating that the simulation has a realistic sea surface height gradient associated with the jet. West of 127°W, however, the modeled sea surface height gradient is weakened or reversed compared with the observations. Along tracks 206 and 171, the simulated sea level at the model's open western boundary is lower than observed by approximately 0.1 m. These differences from observations are passed to the OCTZ model from NCOM-CCS. The overall mean sea surface height gradients along the tracks
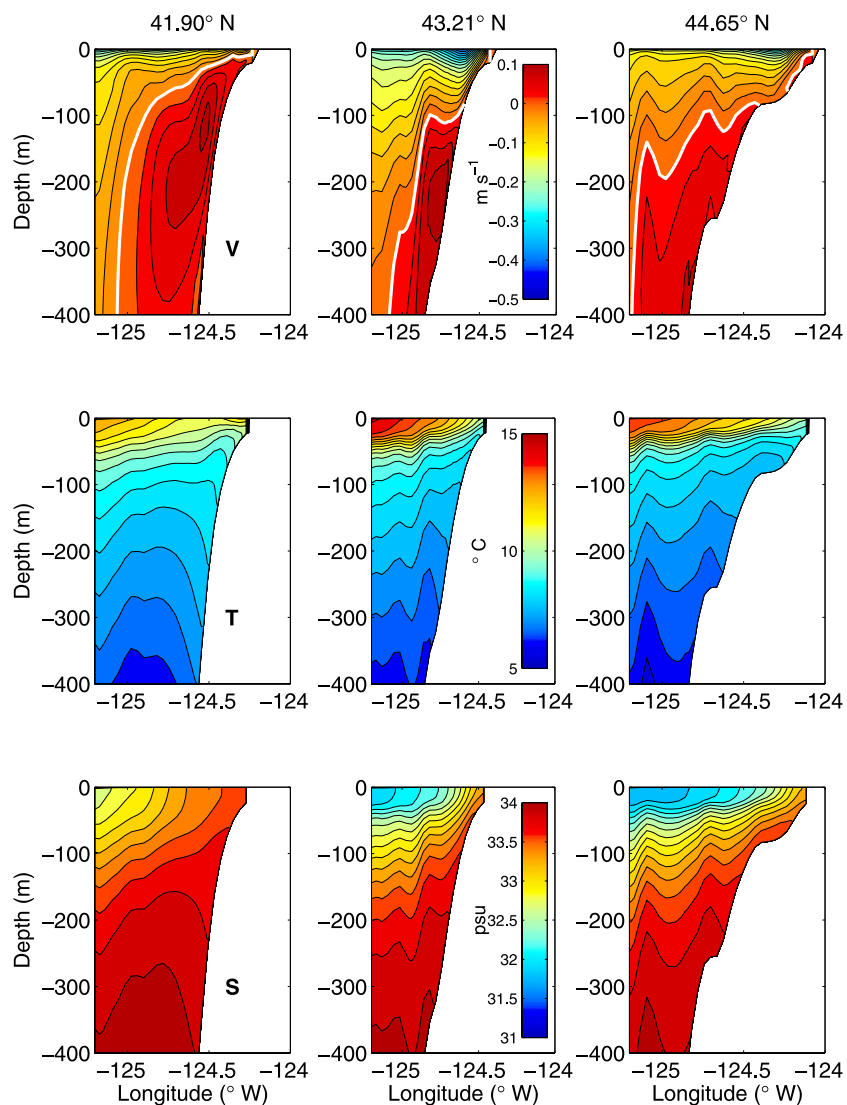
Figure 5. Time mean (days 121–305) of the alongshore velocity (m s^{-1}), temperature (°C), and salinity (psu) on three zonal sections at Crescent City (41.9°N), Coos Bay (43.21°N), and Newport (44.65°N). The zero contour is indicated by a white contour in the velocity plot.

are nearly identical in the two simulations (Figure 6); indeed, imparting large-scale pressure gradients is one of the motivations for nesting a model.

[17] The upwelling front and coastal jet evolve extensively over the course of the OCTZ simulation. Early in the spring, the jet roughly follows the shelf break (200 m isobath, nominally). By day 170 (Figure 7a) the coastal jet separates from the 200 m isobath near the tip of Cape Blanco and follows a meandering path over deep water more than 100 km offshore. The meandering current forms an elongated loop that reaches more than 200 km offshore near 42°N by day 200 (Figure 7b) and detaches as an isolated eddy by day 260 (Figure 7d). This cyclonic eddy encloses a core of the relatively cold and saline water characteristic of the shoreward side of the front (not shown) and moves slowly offshore. Other, smaller eddies form near 44°N and 46°N during this period. Although these mesoscale features are poorly sampled by the sparse satellite coverage, a general comparison of their scale and location is possible. On day 230, for example, the modeled and observed

sea surface height features along track 247 have similar peak-to-trough amplitudes and along-track spatial scales (Figure 8a), and the model produces an offshore trough at nearly the correct location (Figure 7c). Along track 206 a sea surface height front of similar magnitude is seen in both the model and observations, but it is several tens of kilometers farther offshore in the observations than in the model (Figure 8b). In general, the position of meanders or eddies along both tracks differs between the model simulation and the observations; however, in view of the fact that these features result from complex interactions, possibly due to instabilities, exact comparisons cannot be expected.

[18] In addition to mesoscale variability, sea surface height in the OCTZ undergoes a domain-wide increase over the course of the model integration (Figures 7a–7d). Since this gain is of large spatial scale, it can be evaluated by comparing modeled and observed sea surface height spatially averaged independently along each TOPEX/Poseidon track (Figure 9). The model-simulated, along-track-averaged sea surface
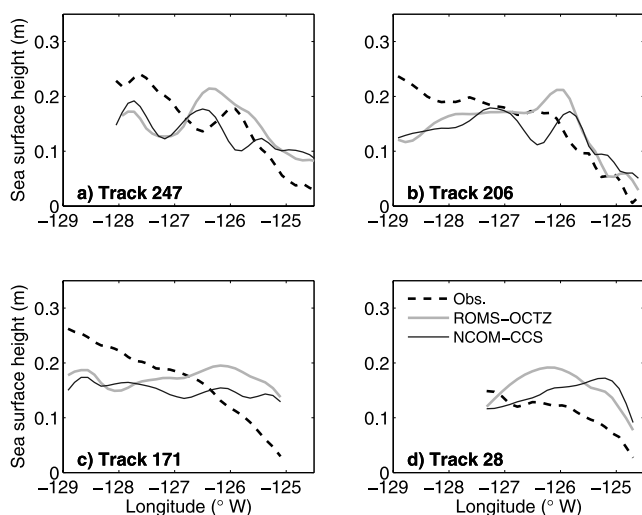
Figure 6. Time averages (days 121–305) of sea surface height along TOPEX/Poseidon tracks (Figure 1a). Dashed lines show values from the absolute dynamic topography, solid gray lines show values from the OCTZ model, and thin black lines show values from NCOM-CCS. The abscissa is labeled by longitude, but all of these tracks also cross a range of latitudes due to the inclination of the orbital tracks.

height shows a steady gain. Although the days of peak sea level differ among the tracks, they are generally consistent with the peak of the domain-averaged model-simulated increase, which occurs on day 272 at approximately 0.10 m higher than on day 120. Observed, along-track-averaged sea levels in this region showing a similar trend and a similar summertime increase in dynamic height have been attributed to seasonal heating by *Huyer et al.* [2007]. Because the model reproduces the seasonal trend, correlations between the model and the observed along-track mean height are high, but higher-frequency variations, which are associated with mesoscale variability, are not well correlated and have larger amplitude in the observations than in the simulation.

[19] In order to focus on the mesoscale variability, this seasonal change in sea surface height is reduced by removing a temporal trend from each alongtrack average and then subtracting this trend at each location along the track. The spatial distribution of the temporal standard deviation of detrended sea surface height along the tracks is similar in the OCTZ model simulation (Figure 10a) and observations (Figure 10b). The largest variability in both is concentrated west and south of the tip of Cape Blanco. Both also show enhanced variability southwest of Heceta Bank, but the model simulation also shows enhanced variability northwest of the bank that is not present in the observations. Overall, variability of sea surface height in the OCTZ model simulation is smaller than in the satellite data but larger than in the coarser-resolution NCOM-CCS simulations (Figure 10c).

[20] Variability of other surface quantities is also enhanced in the region off Cape Blanco. Eddy kinetic energy (EKE), defined as $K' = \frac{1}{2}\left((u')^2 + (v')^2\right)$, where $(u', v') = (u, v) - (\overline{u}, \overline{v})$ and the overbar indicates a time average, is large over a region extending approximately 350 km to the southwest of the cape in the OCTZ simulation (Figure 11a). (Note that the western and southern limits of this patch of EKE may be

affected by the sponge layers that lie along the western and southern boundaries.) This enhanced eddy kinetic energy lies along the path of the mean current as it separates from the coast (Figure 4d), so it reflects variability of the separated current. The disturbances are limited to a shallow (less than 50 m deep) layer in the separated jet. Eddy kinetic energy is also enhanced in regions over the shelf, particularly near topographic features on the central Oregon coast and around Cape Blanco. Calculation of geostrophic velocities from sea surface height demonstrates that geostrophic flow accounts for nearly all of the eddy kinetic energy offshore but not all of the eddy kinetic energy over the shelf. The NCOM-CCS simulation also represents enhanced surface eddy kinetic energy in shelf regions, but little extends offshore (Figure 11b).
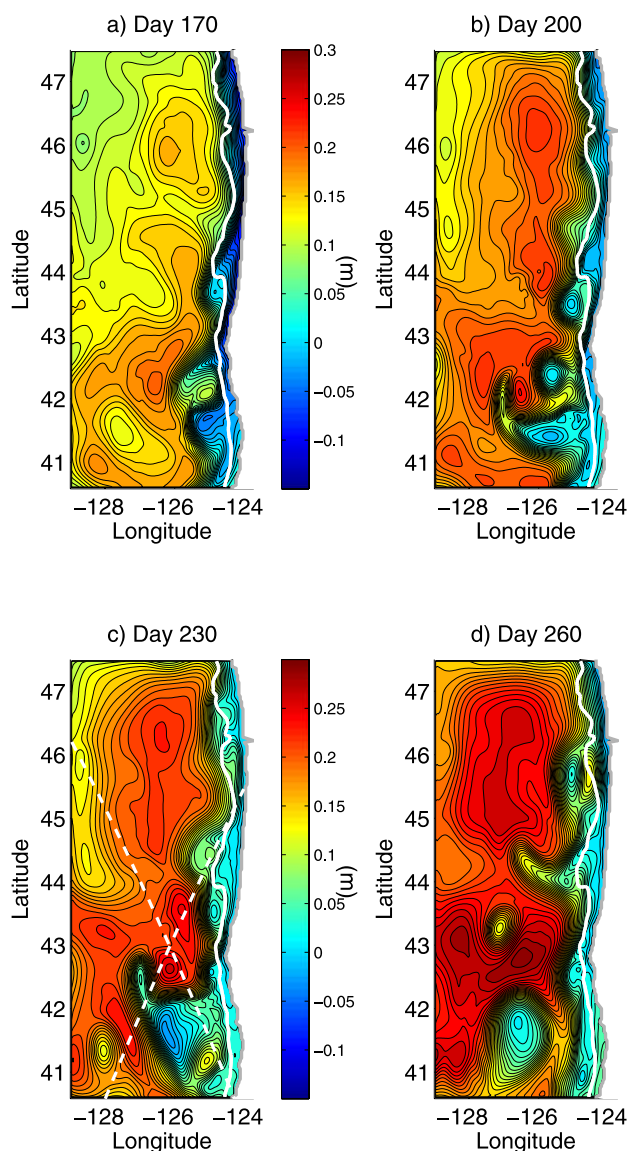

Figure 7. OCTZ model-simulated sea surface height on days 170, 200, 230, and 260. A solid white line indicates the 200 m isobath. The intersecting white dashed lines show TOPEX/Poseidon satellite tracks 206 and 247 (Figure 1a).
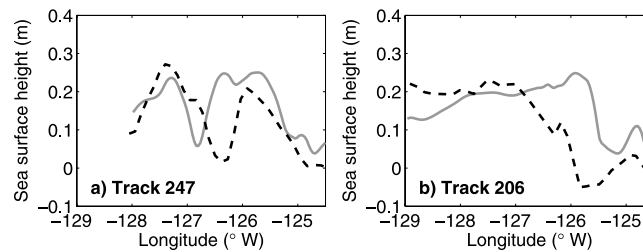
Figure 8. Sea surface height on day 230 estimated from satellite measurements (dashed black line) and model simulation (solid gray line) on tracks (a) 247 and (b) 206.

3.2. Shelf Circulation

[21] Intensive observations along the central Oregon coast, 44.1°N to 45.1°N, make detailed model-data comparisons possible in this region of complex bottom topography. The mean (over days 140–240) currents of the OCTZ model simulation flow southward along the topographic contours to the west of Stonewall Bank and offshore on the northwest side of Heceta Bank (Figure 12b), leaving a region of weak mean currents on the inshore side of the bank. The HF-radar observed jet (Figure 12a) similarly follows the 80 m isobath and then crosses isobaths on the lee side of the bank [*Kosro*, 2005], but it is closer to shore and slightly weaker. After crossing isobaths, the model-simulated jet veers farther offshore so that the SMS mooring (Figure 1b) lies in the quiet region of the model rather than on the inshore edge of the jet as observed. Mean southward surface currents also lie adjacent to the coast, although in the model simulation these are too weak in the north and too strong in the south. As measured by standard deviation, speed in both the jet and the nearshore region show more variability in the model than the HF radar measurements (Figure 12e). The amplitude of the complex correlation [*Kundu*, 1976] is high, and the phase angle is small, indicating that the timing and vector direction

of the modeled and observed surface current variations are similar (Figure 12c). These correlations of surface speeds are greater than 0.7 near all of the mooring locations except SMS.

[22] The strong influence of topography on the flow makes it useful to resolve velocities at the moorings into an along-shelf and a cross-shelf component. These directions are approximated, respectively, by the major and minor axes of variation of the depth-averaged velocities [*Smith*, 1981]. Since currents were not measured within 10–20 m of the top and bottom of the ocean, depth averages for the model also exclude these regions. The orientation of the major axis for the model velocities is within 7° of the observed at all moorings except NIS, possibly due to errors in the nearshore bathymetry (Table 1). Owing to the dominant role of wind stress, depth-averaged, model-simulated major axis velocity fluctuations are largely coherent across the moorings, but there are spatial variations in the amplitude with higher speeds at the northern moorings than the southern moorings and inshore relative to offshore (Figure 13). In addition to the several-day timescale of wind-driven fluctuations, speed has a trend, decreasing by day 240 at all moorings and continuing to be weak until day 305 at NH-10. Excluding SMS, where the weak flow is poorly simulated, correlations exceed 0.76
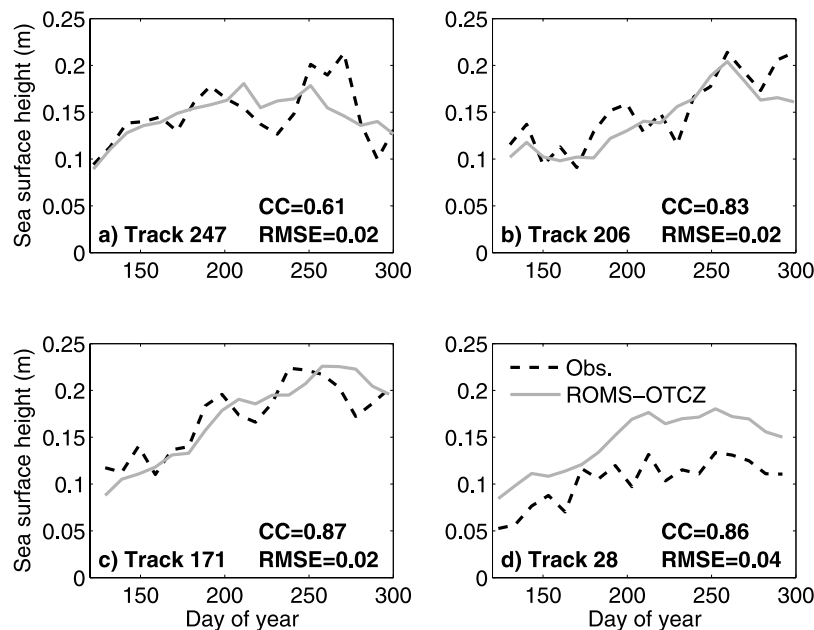

Figure 9. Temporal evolution of sea surface height averaged along TOPEX tracks. The track number is indicated. CC is the correlation coefficient and RMSE is root mean square error. Dashed line is calculated from observations and solid line is calculated from the model simulation.
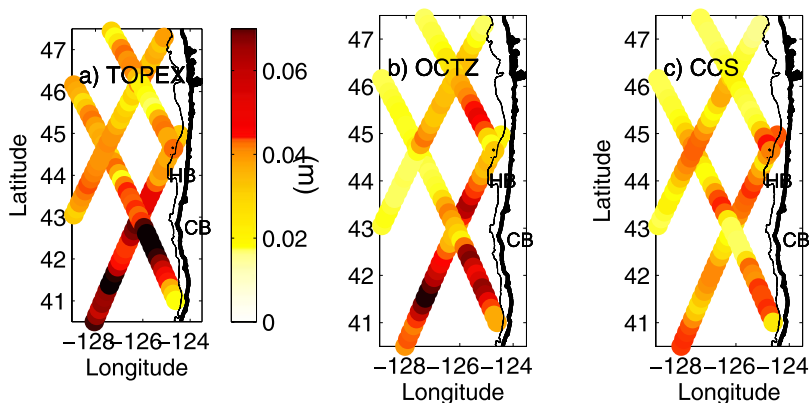
Figure 10. Standard deviation of detrended sea surface height in meters along (a) TOPEX tracks, (b) the OCTZ model sampled along the tracks, and (c) NCOM-CCS sampled along the tracks. The coastline and the 200 m isobath are also shown. HB is Heceta Bank and CB is Cape Blanco.

and RMS errors are less than 0.09 m/s (Table 1). Dividing by the root mean square of the observed velocities gives normalized RMS errors, a measure of noise-to-signal, with smaller values along the northern line of moorings and larger values along the southern line.

[23] Compared with the major axis velocities, the minor axis velocity means and standard deviations are small (generally less than 0.01 m/s and 0.02 m/s, respectively) in both the simulation and the observations (Table 2). The cross-correlations between the OCTZ model and the observations is near zero and the normalized RMS errors exceed one; together, these measures indicate that the model does a poor job of simulating the time-dependent fluctuations in the relatively weak velocities that correspond roughly to across-shelf flow. Difficulty in modeling this component below the mixed layer is consistent with previous experience along the Oregon and California coasts [*Dever*, 1997; *Pullen and Allen*, 2000].

[24] Near-surface temperatures at the moorings show the gradual increase of summertime mixed layer temperature due to surface heat flux modulated by cooling during upwelling events and warming during downwelling events (Figure 14). For example, during an episode of strong northerly winds (Figure 3) on days 219–221, zonal sections from the OCTZ model show isotherms (Figure 15) sloping upward toward the coast, most strongly at the northern section, and becoming nearly vertical. Both the simulated and observed mixed layers are about 20 m deep, but the surface temperature is higher and the temperature gradient at the bottom of the mixed layer is sharper in the observations, which together suggest that the surface heat flux is insufficient. Near-surface temperatures are generally warmer at the shelf break locations compared with the inner shelf locations, and peak between days 240 and 260 (Figure 14). Model simulated and observed surface temperatures have correlations ranging from 0.68 (over the longer time series at NH-10) to 0.92. The observed warming trend at NSB and SSB is not fully reproduced by the model, leading to RMS errors that reach 1.5–2°C.

[25] Because the jet is primarily in thermal wind balance [*Gan and Allen*, 2005a], onshore upsloping of the isotherms implies vertical shear in the along-shelf currents. At NSB, for
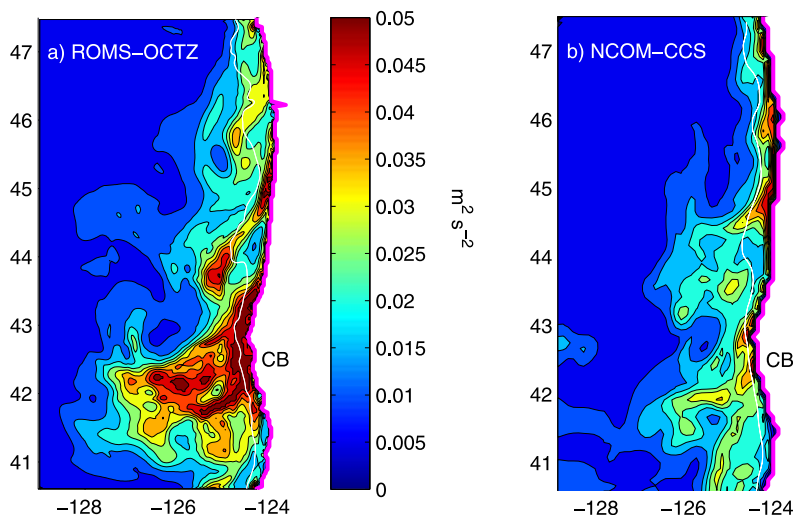

Figure 11. Surface eddy kinetic energy over the interval from day 121 to day 305. The 200 m isobath is shown as a solid white line and Cape Blanco is marked by CB.
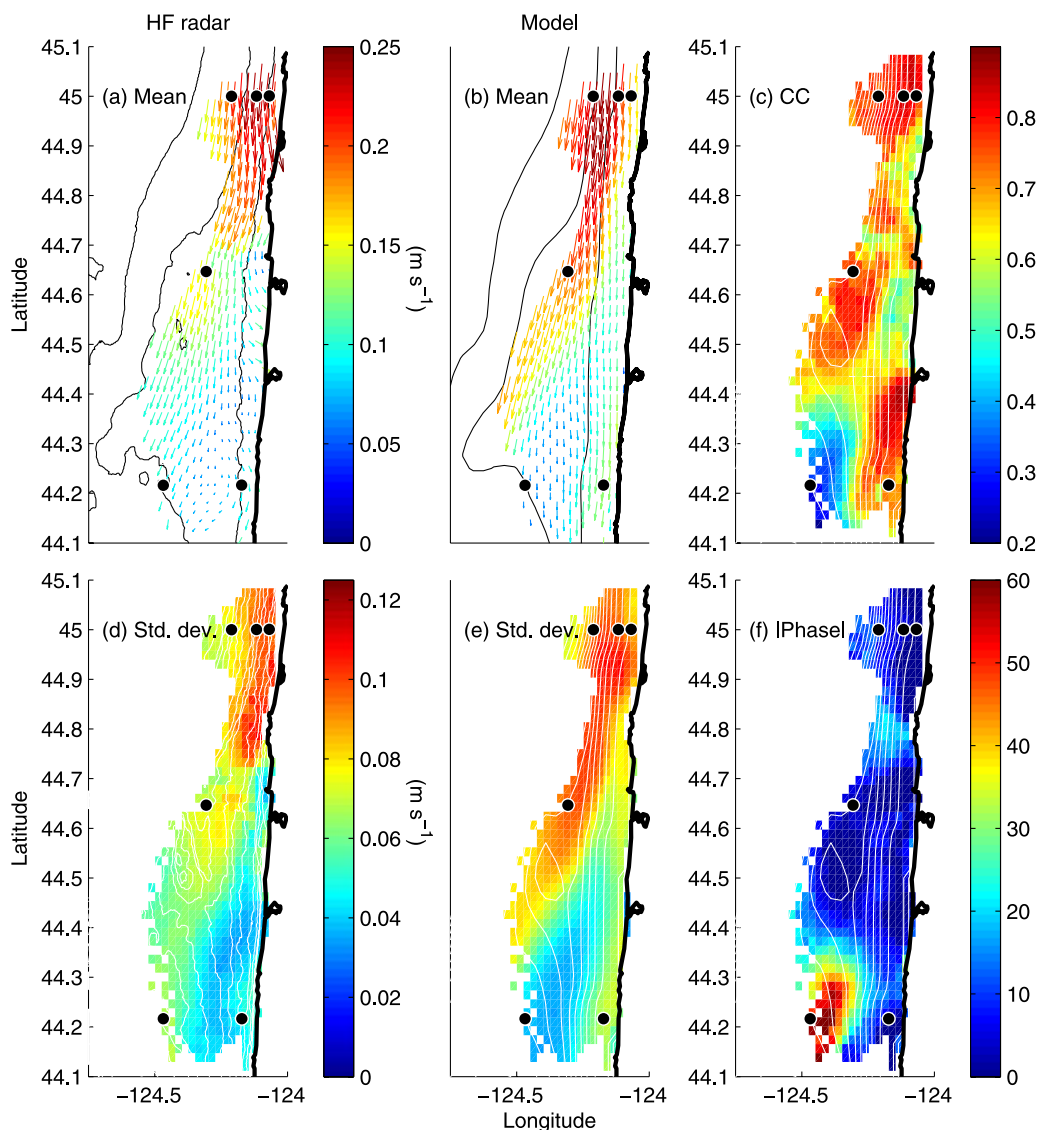
Figure 12. Statistics (days 121–240) for the HF radar array observed [*Kosro*, 2005] and OCTZ model simulated surface velocities. Mean surface speeds and velocity vectors from (a) observations and (b) model. Standard deviations from (d) observations and (e) model. Complex correlations [*Kundu*, 1976] between observations and model: (c) amplitude and (f) corresponding phase angle magnitude (degrees). Bottom depth contours are shown. Black dots indicate positions of moorings (see Figure 1b).

example, the model mean along-shelf velocity decreases from 0.45 m/s at the surface to 0 m/s at 100 m depth (Figure 16). In contrast, the standard deviation of model velocity is more nearly independent of depth. The cross-shelf velocity component at this location is weak in both the mean and in variability. The model's along-shelf velocity has a depth-independent northward bias of approximately 0.03 m/s and larger standard deviation at all depths except near the bottom. Correlations of modeled and observed along-shelf velocity exceed 0.6 at all depths but correlations of across-shelf velocities are small. The modeled and observed mean temperatures are close except in the upper 10 m, where the model is 1°C cooler than the observations, and the modeled standard deviation is larger than observed. Correlations of

modeled and observed temperature reach 0.8 in the upper ocean and are around 0.5 below 40 m.

[26] Tide gauge data gives some idea of the variability along the coastline in areas other than the Heceta Bank region. Comparison of time series of the model-simulated sea level and wind stress shows wind-forced features are highly correlated along the coast (Figure 17). The amplitude of the modeled sea level fluctuations increases from south to north, and, in addition, a trend in sea level occurs over the time period of the model integration, most evidently at North Spit, the southernmost location. Both the long and short timescale changes accurately reflect changes in observed sea level, although there is a model bias of about 0.02 m at most locations and 0.07 m at Toke Point. Without this bias, RMS errors are 0.03–0.05 m. Correlations of
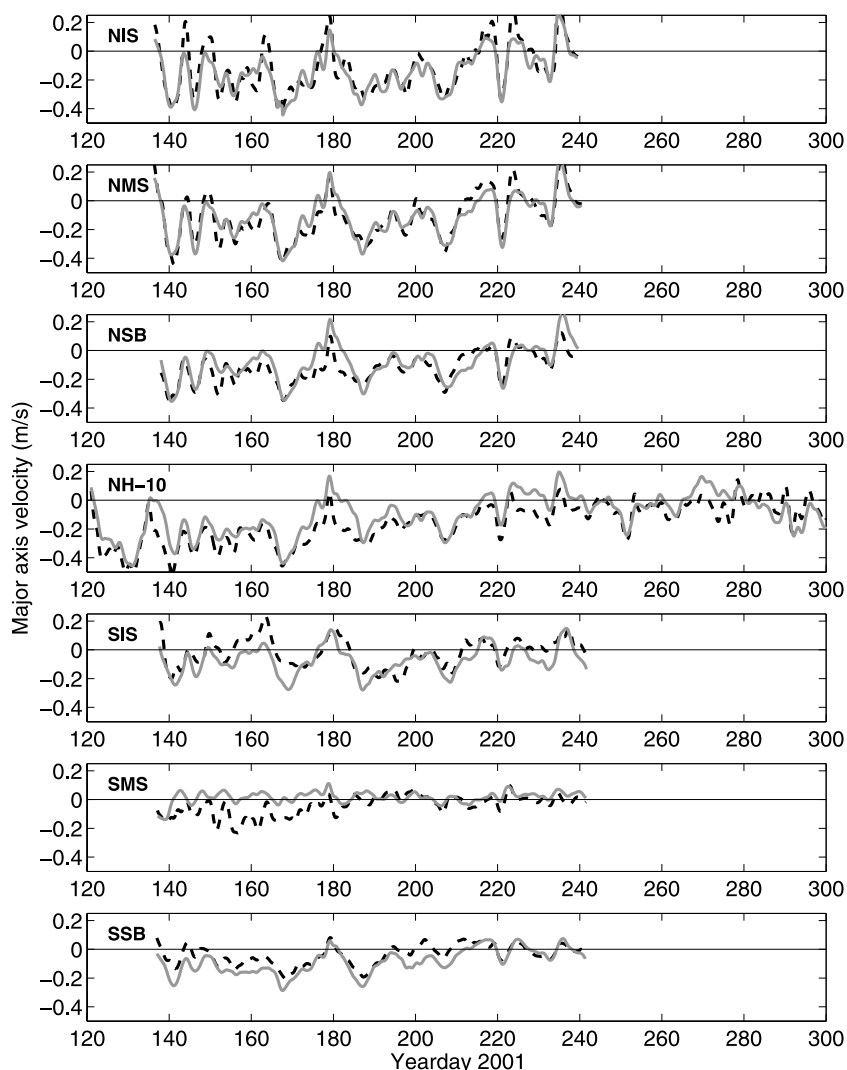
Figure 13. Observed (dashed lines) [*Boyd et al.*, 2002] and OCTZ model-simulated (solid line) vertically averaged velocities in the direction of the major axis of variability. Statistics of the time series are presented in Table 1.

modeled and observed coastal sea level are 0.87–0.89 at all tide gauges except Astoria, a sheltered estuarine location. The coastal sea level statistics in the OCTZ model and in NCOM-CCS are nearly equal (Table 3). It is noteworthy that the OCTZ model performs about as well as NCOM-CCS at North Spit because of its location just north of the southern boundary. This suggests that disturbances

pass successfully into the nested domain from the coarser domain.

4. Analysis of Flow Features

4.1. Coastal Trapped Waves

[27] Exploring the role of coastal trapped waves (CTW) on the circulation on the central Oregon shelf helps differentiate

Table 1. Statistical Properties of the Major Axis Variations of Depth-Averaged Velocities at the Mooring Locations[a]

Mooring Location	Model			Observation			Comparison		
	Mean	Standard Deviation	Angle	Mean	Standard Deviation	Angle	Correlation	RMSE	NRMSE
SSB	−0.084	0.085	28	−0.040	0.066	21	0.85	0.063	0.809
SMS	0.016	0.038	1.7	−0.040	0.068	8.7	0.40	0.085	1.074
SIS	−0.067	0.089	5.2	−0.015	0.091	2.3	0.76	0.081	0.872
NSB	−0.087	0.121	8.4	−0.120	0.102	9.0	0.81	0.079	0.500
NMS	−0.139	0.145	−0.61	−0.141	0.157	8.0	0.90	0.067	0.320
NIS	−0.138	0.147	−5.0	−0.109	0.168	8.8	0.88	0.085	0.423
NH-10	−0.094	0.132	21.2	−0.148	0.133	24.4	0.85	0.089	0.450

[a]See text for definition. Units of mean, standard deviation, and root mean square error (RMSE) are ms^{-1} and angles are degrees counterclockwise from north. Normalized root mean square (NRMSE) is defined as RMSE divided by the root mean square amplitude of the observed velocity signal.

Table 2. Statistical Properties of the Minor Axis Depth-Averaged Velocities at the Mooring Locations[a]

Mooring Location	Model		Observation		Comparison		
	Mean	Standard Deviation	Mean	Standard Deviation	Correlation	RMSE	NRMSE
SSB	0.004	0.017	−0.008	0.018	0.16	0.026	1.294
SMS	−0.007	0.022	0.001	0.041	0.04	0.046	1.137
SIS	−0.001	0.014	−0.018	0.017	0.04	0.027	1.118
NSB	0.006	0.012	−0.004	0.015	−0.12	0.023	1.485
NMS	0.008	0.018	−0.001	0.020	0.01	0.028	1.438
NIS	0.009	0.021	−0.010	0.014	−0.03	0.032	1.834
NH-10	0.002	0.015	−0.006	0.028	0.27	0.029	1.019

[a]Definitions and units are as indicated in Table 1.

the relative importance of wind within the domain and wind south of the domain acting through the open boundary conditions. Subtidal variation in sea level along the western coast of North America can be usefully modeled [*Halliwell and Allen*, 1984; *Battisti and Hickey*, 1984] by a forced and damped, one-dimensional wave equation

$$\frac{1}{c_n}\frac{\partial Y_n}{\partial t} + \frac{\partial Y_n}{\partial y} + \frac{Y_n}{c_n T_f} = b_n \tau(y,t). \tag{1}$$

For each shelf mode n, Y_n represents coastal sea level, c_n is the phase speed, b_n is the projection of the alongshore wind stress, τ, onto the mode, and T_f is a frictional damping timescale. For comparison with the model simulations, we computed solutions to (1) with forcing τ from the meridional COAMPS wind stress averaged over a 50 km strip adjacent to the coast and a southern boundary condition from NCOM-CCS coastal sea level at 40.5°N. Following *Halliwell*
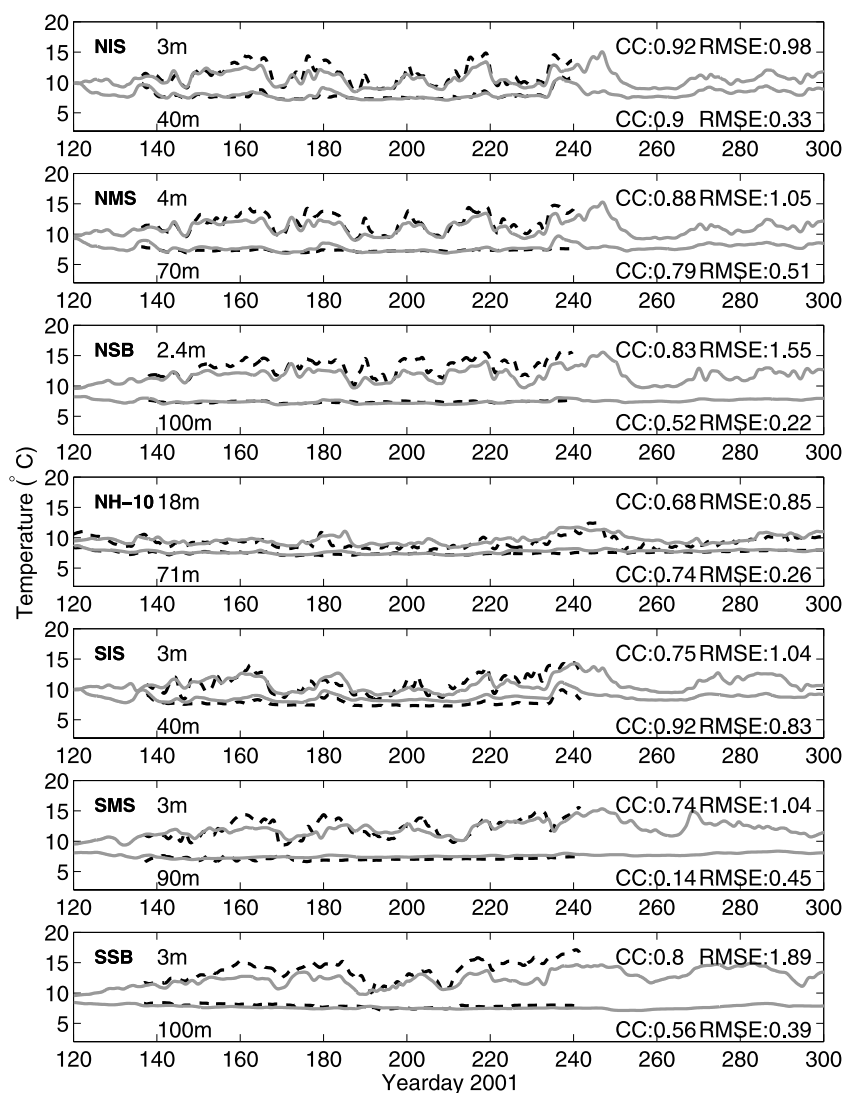

Figure 14. Near-surface and near-bottom temperatures measured at the COAST moorings (dashed line) [*Boyd et al.*, 2002] and simulated in the OCTZ model (solid gray line). Cross-correlation coefficients (CC) and root mean square error (RMSE in m/s) between corresponding observed and modeled temperatures are calculated over the time interval in which there are data.
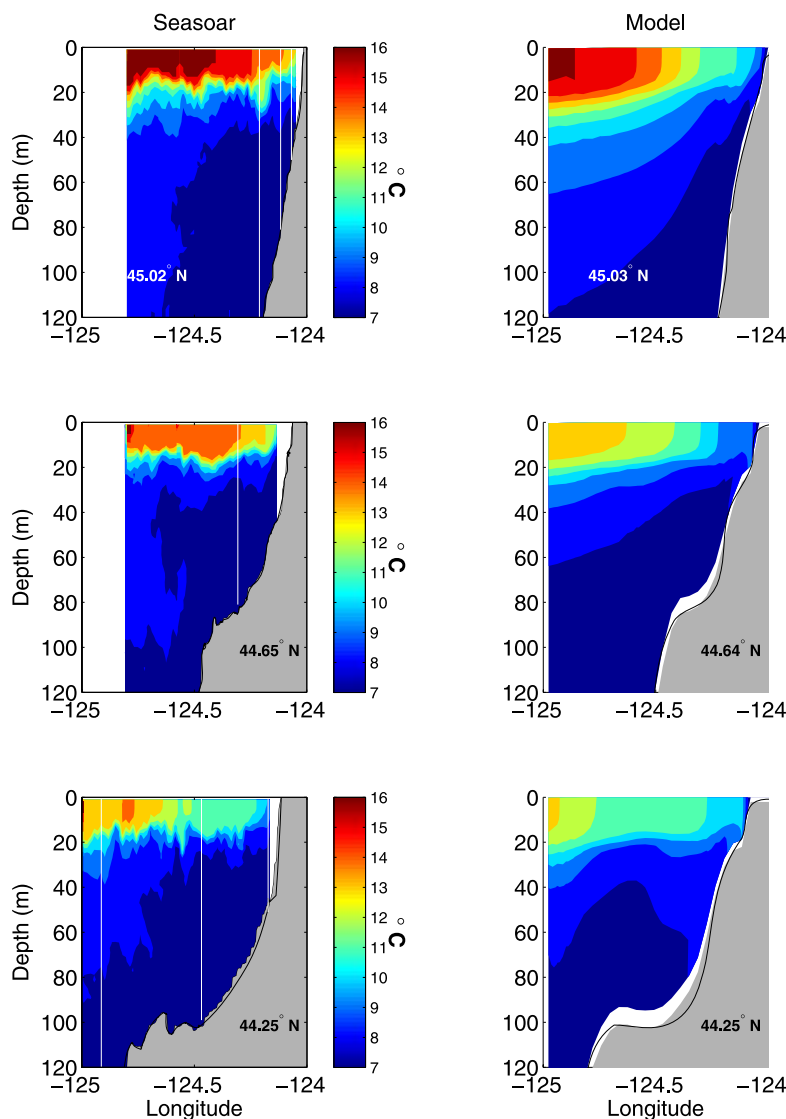
Figure 15. Across-shore potential temperature sections from (left) hydrographic survey on days 219.3–220.8 [*Barth et al.*, 2005] and (right) OCTZ model simulation at 45.25°N, 44.65°N, and 44.25°N on day 220.4. The vertical white lines indicate the positions of the moorings.

and Allen [1984], we used a single mode with $c_1 = 3.25 \, \mathrm{m \, s^{-1}}$, $T_f = 4.25$ days, and $b_1 = 1.19 \times 10^{-6} \, (\mathrm{N \, m^{-2}})^{-1}$.

[28] The CTW model explains most of the variance in coastal sea level. At the South Beach tide gauge (Figure 1b), it reproduces sea level variability as well as the OCTZ model (Figure 18a). As in the OCTZ model, cross correlations between the CTW model and observations are larger and RMS differences are smaller in the southern half of the domain, but these statistics degrade more abruptly for the CTW model than the OCTZ model in the northern part of the domain (Table 3). The simplicity of the CTW model makes it possible to separate the effects of boundary conditions and regional forcing on the coastal sea level by varying the boundary conditions or forcing only in restricted regions. The trend arises mostly from the southern boundary condition (Figure 18b), meaning that it results from changes in sea level outside the OCTZ domain. Although the boundary condition contributes at the frequencies of wind variability, the largest part of the signal results from orographically intensified winds within the domain, between 40.5°N and 42.75°N. Additional wind-forcing between 42.75°N and the tide gauge enhances the signal further. The contributions of these various components of the signal can be quantified by the percent of observed variance explained after demeaning the time series. At South Beach, the southern boundary condition contribution is 53%, the boundary condition plus forcing to 42.75°N is 77%, and the total wave model, including forcing between 42.75°N and the location of the South Beach tide gauge is 73%, a slight degradation. At tide gauges farther to the north, the contribution of the southern boundary condition becomes less important and the winds north of Cape Blanco become more important (not shown). The worsening of the representation of sea level in the northern part of the domain may be due to errors in the wind stress north of South Beach or to spatial variability in the appropriate parameters for the wave model.
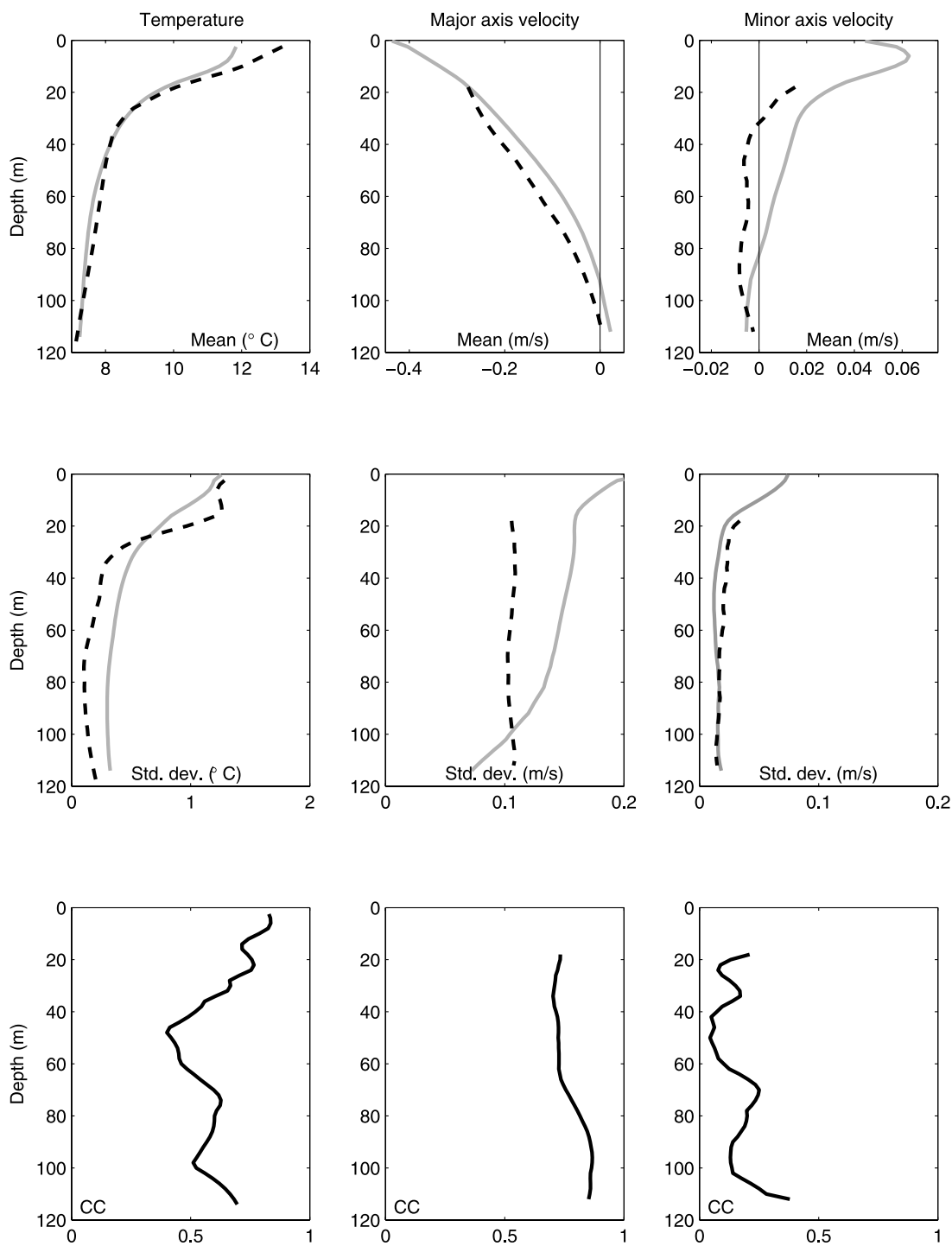
Figure 16. Depth profiles of the statistical properties of T, major axis velocity, and minor axis velocity at NSB. The dashed line is the observed value [*Boyd et al.*, 2002] and the solid gray line is the OCTZ model-simulated value. Positive minor axis velocities are offshore. CC indicates cross-correlation coefficient.

[29] A CTW model can also be applied to alongshore velocities [*Battisti and Hickey*, 1984]. At low frequencies, the geostrophic balance holds, so an estimate of the cross-shelf structure of the CTW modes must be obtained to calculate the derivative of pressure. Because of the complex topography in the Heceta Bank region, we did not use a dynamical CTW mode but instead we used the first mode of a multivariate EOF analysis of the OCTZ model output. The relative weights of this EOF at the mooring locations (Table 4) are generally consistent with the expected dynamical mode structure, with stronger weighting closer to shore and at the northern mooring line, where the shelf is relatively narrow. Additional free parameters in the CTW equation for velocity are a scaling factor for the conversion of pressure to
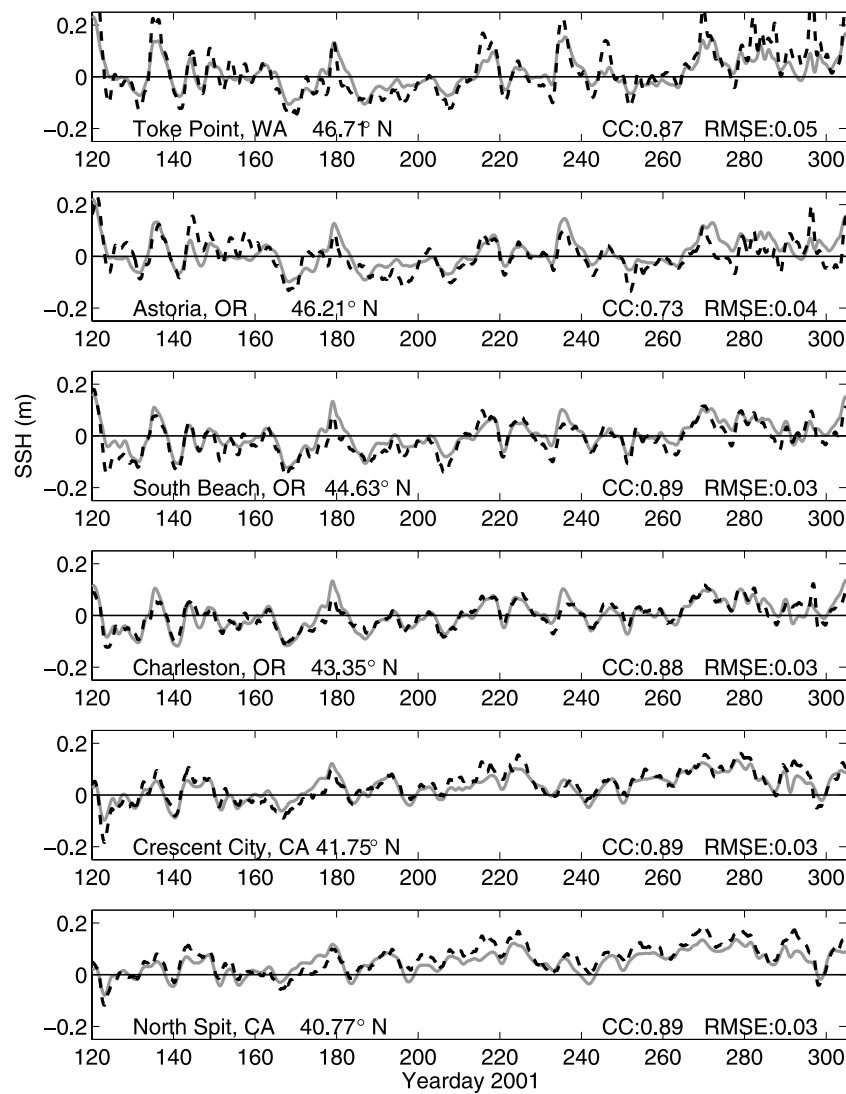
Figure 17. Low-pass filtered sea level (with bias removed) measured at tide gauges (dashed black) and sampled from OCTZ model simulation (solid gray). CC is cross correlation coefficient and RMSE is root mean square error. Time period is entire duration of the model simulation.

velocity, and the weighting of the boundary condition. These parameters were selected here, within reasonable bounds, to fit the observations. The boundary condition is the vertically averaged meridional velocity on the 100 m isobath at the

southern boundary. Since the first mode of the wave model is quasi-barotropic on the shelf, we compare the CTW model with the depth-averaged, major axis velocities. The wave model does not explain the trend in velocity noted earlier. For

Table 3. Statistical Properties of Sea Level in the OCTZ Model and the CCS Model Compared With Tide Gauge Observations (Obs.), the One-Dimensional Wave Model (CTW) Compared With Tide Gauge Observations (Obs.), and OCTZ Model Compared With CTW Modeled Sea Level[a]

Tide Gauge	Latitude (°N)	ROMS OCTZ Versus Obs.		NCOM-CCS Versus Obs.		CTW Versus Obs.		CTW Versus OCTZ at Tide Gauge Locations	
		Corr.	RMSE	Corr.	RMSE	Corr.	RMSE	Corr.	RMSE
Toke Point	46.71	0.87	0.09	0.83	0.11	0.56	0.09	0.83	0.05
Astoria	46.21	0.73	0.06	0.64	0.07	0.47	0.06	0.86	0.05
South Beach	44.63	0.89	0.03	0.88	0.04	0.83	0.03	0.92	0.03
Charleston	43.35	0.88	0.03	0.88	0.03	0.88	0.02	0.94	0.02
Crescent C.	41.75	0.89	0.04	0.90	0.04	0.87	0.03	0.94	0.02
North Spit	40.77	0.89	0.04	0.89	0.03	0.90	0.03	0.92	0.02

[a]RMSE is root mean square error including bias (meters) and Corr. is correlation coefficient.
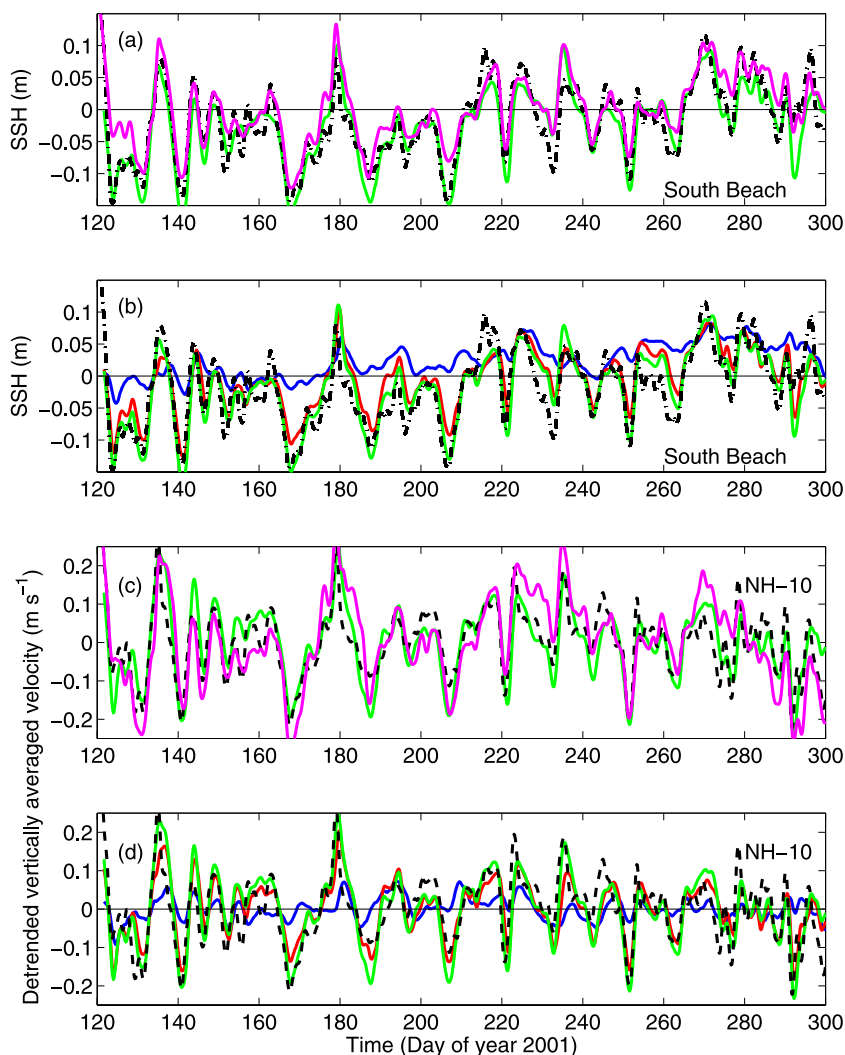
Figure 18. (a) Coastal sea level at South Beach, Oregon, as measured by tide gauge (black dashed), and as simulated by OCTZ model (magenta) and by one-dimensional wave equation (green). (b) Contributions of wave forcing along wave characteristic at the tide gauge. Blue indicates the southern boundary condition, red indicates the addition of wind forcing between 40.5°N and 42.75°N, and green indicates the addition of wind forcing between 42.75°N and 45°N. (c) Detrended, vertically averaged velocity at NH-10 as measured (black dashed), simulated by OCTZ model (magenta), and modeled by wave equation (green). (d) As in Figure 18b, but for velocities at NH-10.

Table 4. Statistical Properties of Detrended Principal Axis Velocities in the OCTZ Model (ROMS) Compared With Those at the Moorings (Obs.), the One-Dimensional Wave Model (CTW) Compared With Tide Gauge Observations (Obs.), and ROMS Compared With CTW Modeled Sea Level[a]

Mooring Location	EOF Weight	ROMS OCTZ Versus Obs.		CTW Versus Obs.		CTW Versus ROMS OCTZ	
		Corr.	SDE	Corr.	SDE	Corr.	SDE
NSB	0.7192	0.76	0.04	0.88	0.05	0.88	0.05
NMS	1.0000	0.89	0.06	0.88	0.07	0.91	0.06
NIS	1.0495	0.87	0.06	0.81	0.10	0.87	0.08
NH-10	0.6481	0.79	0.07	0.78	0.06	0.76	0.07
SSB	0.3222	0.83	0.06	0.72	0.04	0.85	0.03
SMS	0.0651	0.31	0.08	0.21	0.05	0.21	0.04
SIS	0.6692	0.76	0.07	0.58	0.09	0.80	0.06

[a]These differ from the numbers in Table 1 because the trend has been removed. STDE is standard deviation of error (ms^{-1}), which is root mean square error after the mean is removed, and Corr. is correlation coefficient.

this reason, the temporal trend is removed from the observed data and OCTZ model data for comparison with the wave model predictions.

[30] At the frequency of wind events, the velocity comparison at NH-10 is similar to the coastal sea level comparison at South Beach (Figure 18c). On several occasions during the middle of the summer, the observed velocities did not respond as strongly to upwelling favorable winds as predicted by the wave model, although coastal sea level did. Without a long-term trend, as seen in sea level, the contribution of the southern boundary condition to the depth-averaged velocity variance is much smaller (Figure 18d), explaining 8% of the observed variance at NH-10. This result suggests that freely propagating waves originating from south of Cape Mendocino play a small role in velocity fluctuations on the central Oregon coast. The boundary condition plus the forcing south of Cape Blanco explains 50% of the observed variance, indicating that the orographically enhanced winds in this region have an important effect on the velocities near Heceta Bank. Adding the forcing north of Cape Blanco increases the percent of observed variance explained to 53%, so the winds between 42.75°N and 44.65°N, the latitude of the mooring, contribute relatively little. Because of the similarity of the wave model and OCTZ model predictions for velocity (Table 4), the relative importance of these contributions is assumed to be similar in the OCTZ model.

4.2. Lagrangian Pathways From Shelf to Open Ocean

[31] The present simulation resolves a broad range of shelf, slope, and offshore scales of motions and provides a new opportunity to investigate the complex three-dimensional Lagrangian motions that are associated with the coastal upwelling circulation and the interaction of shelf-scale processes with the slope and interior. In addition to their intrinsic physical interest, these Lagrangian pathways are of particular importance for biological processes and ecosystem dynamics. The separation of the coastal jet at Cape Blanco, for example, has a major impact on the offshore extent over which ecosystems can be influenced by nutrient enhancement due to coastal upwelling [*Peterson and Keister*, 2002]. For this reason we focus on the origin of the waters that form the meanders and eddies offshore of Cape Blanco.

[32] The active tracers in the model, temperature and salinity, indicate the location of upwelled water, but they do not show where or when it upwelled. For this purpose, it is useful to define Lagrangian labels $X(x, y, z, t)$, $Y(x, y, z, t)$, and $Z(x, y, z, t)$, satisfying the following equations:

$$\frac{DX}{Dt} = 0, \quad \frac{DY}{Dt} = 0, \quad \frac{DZ}{Dt} = 0, \qquad (2)$$

where $D/Dt = \partial/\partial t + u\partial/\partial x + v\partial/\partial y + w\partial/\partial z$. With the initial conditions at $t = t_0$

$$X(x, y, z, t_0) = x, \quad Y(x, y, z, t_0) = y, \quad Z(x, y, z, t_0) = z, \qquad (3)$$

these labels give the initial x, y, and z (longitude, latitude, and depth) locations, respectively, of the parcels that are advected by the model-resolved velocity field and are parcels found at positions (x, y, z) at time t [*Kuebel Cervantes et al.*, 2003; *Kuebel Cervantes and Allen*, 2006]. At any location and time,
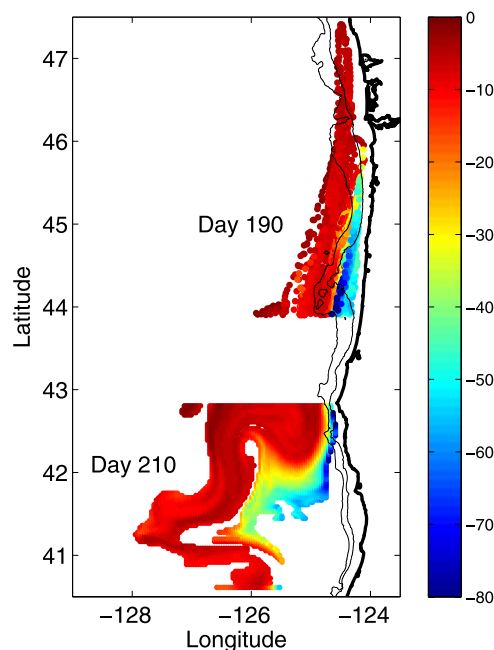

Figure 19. Lagrangian label tracer location on day 190 (north of 44°N) and the same patch of tracer at the surface on day 210 (south of 42.8°N). At both times color corresponds to the depth of the tracer on day 190. The white spaces between the dots on day 190 arise because the inverse mapping to initial positions does not preserve continuity. The white spaces on day 210 indicate regions where the water at the surface did not originate north of 44°N within the given time frame.

the initial position can be determined by examining the Lagrangian label. The evolution of the label fields is calculated on the model grid at every time step using the model velocity field and the same horizontal and vertical advection schemes used for temperature and salinity. However, the label tracers are not subject to diffusion; thus, the interpretation of these labels can be ambiguous with regard to unresolved small-scale velocities on Lagrangian parcel paths if the inferred trajectories pass through regions of strong turbulent mixing, such as the surface and bottom boundary layers over the shelf.

[33] Lagrangian labels help identify the pathways of water parcels during the strong, upwelling-favorable winds that dominate from day 190 to day 210 (Figure 3). Water located at the sea surface south of Cape Blanco on day 210 that originated north of 44°N, for example, can be identified, and its initial and final positions mapped (Figure 19). The results suggest that this fluid originates over the Heceta Bank region and over the northern Oregon shelf and slope and that the inshore portion of fluid has upwelled from depths of 50 to 80 m, while the offshore portion originated at the surface on day 190. Overall, the label calculation indicates that the fluid at the surface on day 210 that has upwelled from depths greater than 20 m on day 190 is primarily found on day 210 over the southern shelf and slope, south of Cape Blanco, and extending offshore past 126°W (Figure 20).

[34] These inferences about relationship between the shelf circulation and the separated current south of Cape Blanco are qualitatively consistent with observations. Surface drifters deployed over the shelf along 44.65°N during July
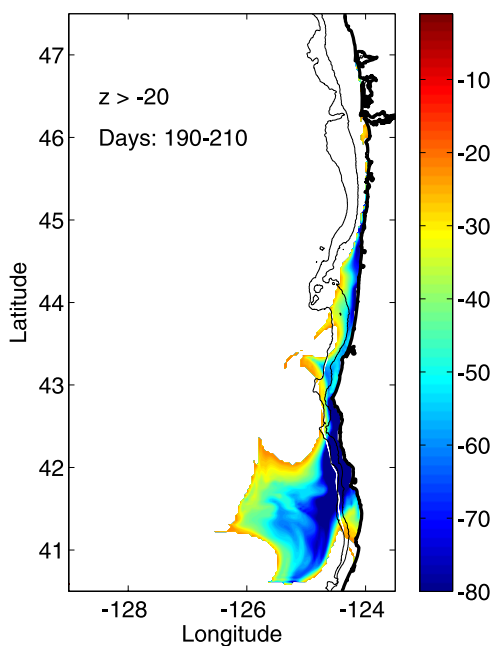
Figure 20. All Lagrangian labels that were deeper than 20 m on day 190 but are at the surface on day 210. Colors correspond to depth on day 190. Compared with Figure 19, the additional area of upwelled water in the south is due to upwelling that occurred south of Cape Blanco rather than around Heceta Bank.

of 2000–2003 moved southward in the coastal jet and followed it offshore near Cape Blanco [*Barth*, 2003]. Isopycnal floats deployed beneath the mixed layer north of Heceta Bank in 2000 and 2001 also moved generally southward [*D'Asaro*, 2004]. Some were advected onshore and upward, consistent with upwelling, while others followed a path around the outer edge of Heceta Bank and reached the surface near Cape Blanco.

4.3. Effects of Perturbed Initial Conditions

[35] The significance of detailed model-data comparisons presented earlier depends in part on the predictability of the flow. Here we test sensitivity to initial conditions by considering a small ensemble consisting of the original simulation plus four additional simulations that are initialized from corresponding time-dependent fields in NCOM-CCS 10 and 20 days earlier and later.

[36] The effect of the perturbation in initial conditions on the solutions varies spatially. Differences between sea surface height in model runs in the ensemble are small on the shelf; for example, at each tide gauge correlations vary by less than 0.06 and RMS errors relative to observations vary by less than 0.008 m between ensemble members (Table 5). For depth-averaged velocities, differences in correlations tend to be smaller closer to shore and larger toward the shelf break (Table 6). Seaward of the 200 m isobath, differences between the model runs grow over time, and the divergence of the solutions is quantified by the ensemble standard deviation of sea surface height (Figure 21). On day 170 the differences begin in a small region primarily west of Cape Blanco and Heceta Bank as deviations in the path of the coastal jet, and over time large values of ensemble standard deviation

spreads northward and westward. The peak value of 0.12 m occurs on day 260 (Figure 21d) and represents differences in the position of the large cyclonic eddy, which is recognizable in all members of the ensemble but occurs in different locations to the southwest of Cape Blanco. The domain-averaged ensemble standard deviation in sea surface height grows at a nearly linear rate throughout the course of the integration, increasing from 0.005 m on day 140 to 0.025 m on day 305.

[37] Although details of the circulation are affected by the initial conditions, the differences between model runs are localized. This localization is demonstrated by averaging the surface total kinetic energy in three regions: a coastal region east of 125°W, a southern offshore region west of 125°W and south of 43.5°N, and a northern offshore region west of 125°W and north of 43.5°N. Differences in surface total kinetic energy averaged over the coastal region are small until after day 200 and are always much smaller than the fluctuations in the ensemble mean (Figure 22), indicating that the shelf flow is strongly controlled by the wind-forcing. In the southern offshore region, which lies west of Cape Blanco, all model runs in the ensemble show a similar increase in average kinetic energy from initialization to roughly day
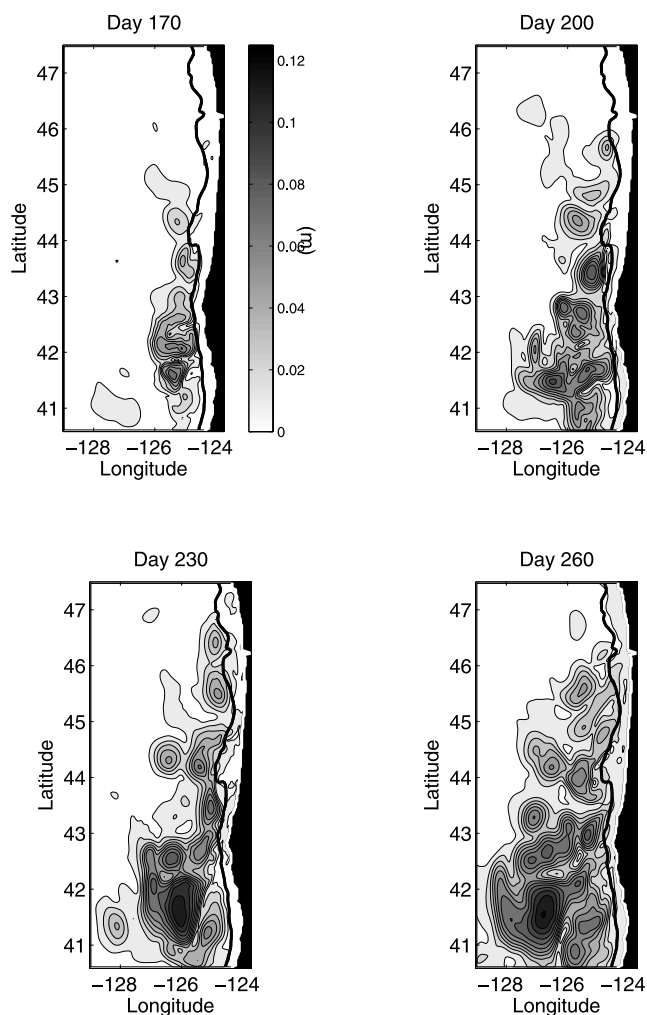

Figure 21. Ensemble standard deviation of sea surface height for model runs initialized on different days. The solid black line shows the 200 m isobath.

Table 5. Minimum and Maximum Statistical Properties of Sea Level at Tide Gauge Locations for Members of the Initial Condition Ensemble Over the Period From Day 140 Through Day 305[a]

	Toke Pt.		Astoria		South Beach		Charleston		Crescent C.		North Spit	
	Min.	Max.	Min.	Max.	Min.	Max.	Min.	Max.	Min.	Max.	Min.	Max.
Correlation	0.86	0.87	0.68	0.74	0.86	0.89	0.86	0.89	0.86	0.89	0.84	0.89
RMSE	0.049	0.052	0.043	0.046	0.029	0.033	0.025	0.028	0.027	0.031	0.029	0.037

[a]Units of root mean square error (RMSE) are meters.

200–210, followed by a slow decrease, with relatively little indication of direct response to wind variability. The ensemble spread is initially small but expands around day 180 and stays constant thereafter. The northern region has lower surface kinetic energy, which increases only slowly over the simulations, and ensemble standard deviations remain small. Although the precise time and location of mesoscale features is unpredictable, the seasonal peak and the general location in a region west of Cape Blanco and south of Heceta Bank are robust characteristics.

5. Discussion

[38] A number of previous numerical modeling studies have simulated circulation on the central Oregon shelf during summer upwelling conditions [*Oke et al.*, 2002a, 2002b; *Kurapov et al.*, 2005a, 2005b; *Gan and Allen*, 2005a]. These studies concentrated primarily on the Heceta Bank region and covered a time interval roughly equivalent to half of that used here. Although the results are not directly comparable because of the difference in time period, their depth-averaged velocity correlations in the mooring array were all less than 0.7, and the RMS errors were 0.03–0.05 m/s larger than those given here. Correlations and errors in the temperatures at the moorings were comparable to those found here. *Kurapov et al.* [2005b] demonstrated other deficiencies in model coastal sea level, surface velocities, and stratification. They showed that assimilation of moored velocities improved accuracy. After assimilation, the statistics of their comparisons were similar to those obtained by the nonassimilating OCTZ model presented here.

[39] Major limitations of these previous models are the use of periodic conditions on the northern and southern boundaries and the use of spatially uniform winds. To address these issues, *Gan et al.* [2005] applied open boundary conditions at the northern and southern boundaries and forced the model with spatially variable winds from a mesoscale atmospheric model [*Samelson et al.*, 2002]. Improvements in the simulation of amplitude and phase of velocities measured at the moorings on the mid-Oregon shelf were attributed to coastal trapped waves generated by enhanced strength and variability of wind stress south of Cape Blanco [*Perlin et al.*, 2004]. Because the southern boundary condition was determined by solutions to a two-dimensional (zonal slice) model, incident coastal-trapped wave energy from south of the domain was not represented. In the present simulation the boundary condition formulation used for the nesting in the present simulation allows incident coastal trapped wave energy to propagate into the inner model domain at the southern boundary.

[40] An additional limitation of the previous models is the use of spatially uniform stratification and zero motion at initialization. These earlier model studies focused on shelf flows, which spun up in response to wind-forcing within days. Deeper flows, such as the coastal undercurrent, did not develop within the time frame of the model integration. However, when the nested grid model was initialized from a California Current System model that included these features, they were sustained in the OCTZ model through the period of integration. Longer integrations are necessary to determine whether subsurface features can be adequately maintained by a combination of forcing within the nested domain and boundary conditions.

[41] The well-defined separation of the jet from the coast in the vicinity of Cape Blanco found in observations is a new feature in a regional model of the OCTZ. The separation process appears to be rather complex and understanding of the exact physical mechanisms involved remains incomplete. Recent hypotheses have focused on how local effects cause enhanced upwelling that advects the surface currents offshore downstream of the cape. *Barth et al.* [2000], *Dale and Barth* [2001], and *Castelao and Barth* [2006] explored the hypothesis that separation occurs when the jet encounters topographic features along the shelf and slope near Cape Blanco. An alternative hypothesis is that orographic intensification of wind flowing over the cape contributes to separation [*Samelson et al.*, 2002]. Idealized experiments [*Castelao and Barth*, 2007] and a realistic simulation [*Gan et al.*, 2005] including intensification of winds around the cape demonstrated separation of the jet, but it reattached to the coast less than 100 km south of Cape Blanco rather than forming a free oceanic jet. *Castelao and Barth* [2007] suggest separation may have been inhibited by the southern boundary conditions, which did not specify the existence of an offshore jet. The southern boundary conditions for the present model simulation do represent the separated coastal jet because NCOM-CCS represents separation. Further research is needed to determine the relative importance of topographic features, spatial variation

Table 6. As in Table 5, but for Major Principal Axis Velocities at the Mooring Locations[a]

	NIS		NMS		NSB		SIS		SMS		SSB	
	Min.	Max.	Min.	Max.	Min.	Max.	Min.	Max.	Min.	Max.	Min.	Max.
Correlation	0.82	0.88	0.79	0.90	0.68	0.82	0.70	0.78	0.07	0.45	0.71	0.83
RMSE	0.081	0.118	0.064	0.086	0.068	0.084	0.082	0.085	0.079	0.088	0.040	0.069

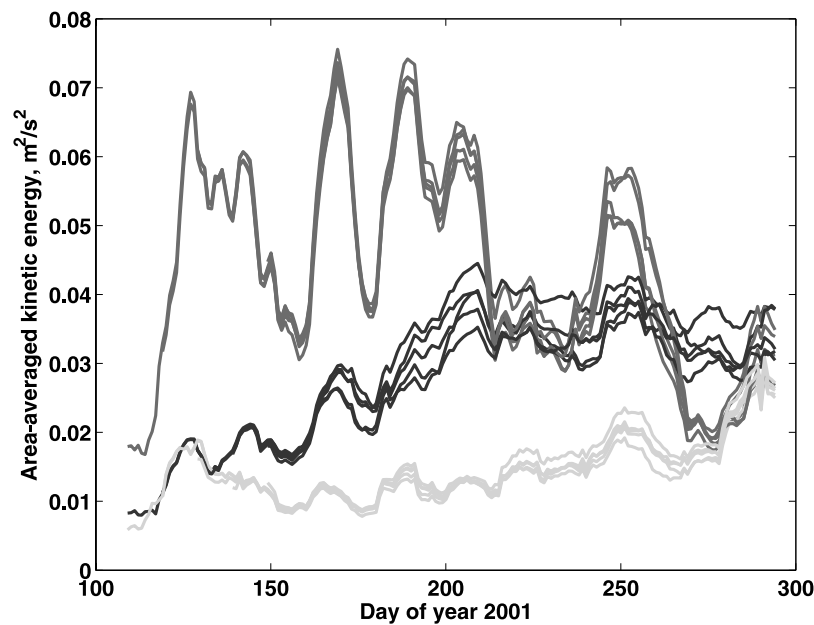[a]Units of root mean square error (RMSE) are m s^{-1}.

Figure 22. Area-averaged surface kinetic energy within three subdomains: medium gray is coastal subdomain, light gray is northern offshore subdomain, and dark gray is southern offshore subdomain (see text for definitions of subdomains). Associated with each subdomain are five lines corresponding to the different members of the ensemble.

of wind stress, and boundary conditions in separation in the nested model.

[42] An additional new feature for an OCTZ model is the development offshore of Cape Blanco of a large region of flow variability that is not directly forced by fluctuations in the winds. This intrinsic variability may arise from instability of the separated current systems. In a larger-scale simulation of the California Current System, *Marchesiello et al.* [2003] identify baroclinic instability of the mean currents as the basic mechanism underlying initiation and growth of mesoscale features in the California Current System. In the present simulation, surface eddy kinetic energy in the 3 km OCTZ model was markedly higher than in 9–10 km NCOM-CCS model, which is consistent with the findings of *Marchesiello et al.* [2003] showing intrinsic variability increased as model resolution was increased from 10 km to 5 km and then to 3.5 km. At their highest model resolution, additional variability arose from a short-wavelength ageostrophic, frontal instability, which gave rise to fast-growing eddies concentrated in the upper water column (<50 m). Very high resolution (1 km or better) model studies of the shelf response to the onset of upwelling favorable winds show the finite amplitude growth of frontal instabilities at the base of the mixed layer with a preferred length scale of 8–10 km growing to larger scales over a period of 10 days [*Durski and Allen*, 2005]. Since the present model simulation cannot resolve these scales, further refinement of the grid may lead to an additional increase in variability.

[43] A consequence of this region of intrinsic variability is that details of the offshore flow are not deterministic. Model data comparisons in the region off Cape Blanco are best limited to statistical rather than detailed point-by-point comparisons. In addition to internal disturbance growth, other sources of unpredictability include errors in initial and boundary conditions, uncertainty or incompleteness in forc-

ing (winds, tides, heat fluxes, freshwater fluxes, and air-sea interaction), and deficiencies in model representation of physical processes arising from inadequate resolution or parametrization of subgridscale processes. Quantification of the relative importance of these sources of error will help focus future efforts in improving simulation and forecasting capabilities in this region. Further improvement will likely depend on assimilation of data, such as surface currents measured by HF radar and sea surface height measured by satellite altimeter.

6. Summary

[44] The present OCTZ simulation reproduces accurately the detailed structure of the shelf flow over the region of complicated topography of Heceta Bank along the central Oregon coast. At the same time, it provides a representation of jet separation and eddy formation in the OCTZ, especially off Cape Blanco, in approximate accord with available observations. The nested OCTZ model simulation improved on the CCS simulation by producing a higher level of variability in the separation region. Lagrangian label tracer calculations allow the identification of the source of upwelled water in the separated jet and eddy features off Cape Blanco, a first step in the modeling and analysis of the cross-shelf exchange of fluid and material that controls the characteristics of the northernmost portion of the California Current System. The ensemble calculations, although limited in scope, suggest that the variability over the shelf is dominated by a deterministic response to wind forcing, but in the Cape Blanco region is a mixture of deterministic response and intrinsic instability of the separated jet.

[45] Differences from observations revealed shortcomings of the nested grid model simulations. The most serious discrepancy is that the mean sea surface height in the northern

part of the domain differs considerably from the absolute dynamic topography product. Owing to the boundary conditions used here, sea surface height on the boundary of the nested model nearly matches that of the model in which it is nested; thus, errors in the large-scale sea surface height of the OCTZ model are due in part to errors in the nonassimilating NCOM-CCS model. Experiments with nesting in a version of NCOM that assimilates upper ocean density show improvement in this regard. Another difficulty is that the sea surface temperature in offshore areas consistently is too high by about 2°C while over the shelf it tends to remain too low. Efforts to improve the surface heat flux in the OCTZ model are under way. Finally, increased resolution in future models is expected to result in better representation of topographic effects on flows, cross-shelf transport, and instabilities on the shelf.

References

Bane, J. M., M. D. Levine, R. M. Samelson, S. M. Haines, M. F. Meaux, N. Perlin, P. M. Kosro, and T. Boyd (2005), Atmospheric forcing of the Oregon coastal ocean during the 2001 upwelling season, *J. Geophys. Res.*, 110, C10S02, doi:10.1029/2004JC002653.

Barron, C. N., A. Birol Kara, H. E. Hurlburt, C. Rowley, and L. F. Smedstad (2004), Sea surface height predictions from the global Navy Coastal Ocean Model during 1998–2001, *J. Atmos. Oceanic Technol.*, 21, 1876–1893, doi:10.1175/JTECH-1680.1.

Barth, J. A. (2003), Anomalous southward advection during 2002 in the northern California Current: Evidence from Lagrangian surface drifters, *Geophys. Res. Lett.*, 30(15), 8024, doi:10.1029/2003GL017511.

Barth, J. A., and P. A. Wheeler (2005), Introduction to special section: Coastal Advances in Shelf Transport, *J. Geophys. Res.*, 110, C10S01, doi:10.1029/2005JC003124.

Barth, J. A., S. D. Pierce, and R. L. Smith (2000), A separating coastal upwelling jet at Cape Blanco, Oregon, and its connection to the California Current System, *Deep Sea Res., Part II*, 47, 783–810, doi:10.1016/S0967-0645(99)00127-7.

Barth, J. A., S. D. Pierce, and R. M. Castelao (2005), Time-dependent, wind-driven flow over a shallow midshelf submarine bank, *J. Geophys. Res.*, 110, C10S05, doi:10.1029/2004JC002761.

Batteen, M. L. (1997), Wind-forced modeling studies of currents, meanders, and eddies in the California Current System, *J. Geophys. Res.*, 102, 985–1010, doi:10.1029/96JC02803.

Battisti, D. S., and B. M. Hickey (1984), Application of remote wind-forced coastal trapped wave theory to the Oregon and Washington coasts, *J. Phys. Oceanogr.*, 14, 887–903, doi:10.1175/1520-0485(1984)014<0887:AORWFC>2.0.CO;2.

Beckmann, A., and D. B. Haidvogel (1993), Numerical simulation of flow around a tall isolated seamount. Part I: Problem formulation and model accuracy, *J. Phys. Oceanogr.*, 23, 1736–1753, doi:10.1175/1520-0485(1993)023<1736:NSOFAA>2.0.CO;2.

Boyd, T. J., M. D. Levine, P. M. Kosro, S. R. Gard, and W. Waldorf (2002), Observations from moorings on the Oregon continental shelf, May August 2001, *Data Rep. 190*, Coll. of Oceanic and Atmos. Sci., Oreg. State Univ., Corvallis.

Brink, K. H., and T. J. Cowles (1991), The coastal transition zone program, *J. Geophys. Res.*, 96, 14,637–14,647, doi:10.1029/91JC01206.

Castelao, R. M., and J. A. Barth (2005), Coastal ocean response to summer upwelling favorable winds in a region of alongshore bottom topography variations off Oregon, *J. Geophys. Res.*, 110, C10S04, doi:10.1029/2004JC002409.

Castelao, R. M., and J. A. Barth (2006), The relative importance of wind strength and along-shelf bathymetric variations on the separation of a coastal upwelling jet, *J. Phys. Oceanogr.*, 36, 412–425, doi:10.1175/JPO2867.1.

Castelao, R. M., and J. A. Barth (2007), The role of wind stress curl in separation at a cape, *J. Phys. Oceanogr.*, 37, 2652–2671, doi:10.1175/2007JPO3679.1.

Chapman, D. C. (1985), Numerical treatment of cross-shelf open boundaries in a barotropic coastal ocean model, *J. Phys. Oceanogr.*, 15, 1060–1075, doi:10.1175/1520-0485(1985)015<1060:NTOCSO>2.0.CO;2.

Choboter, P. F., J. S. Allen, R. M. Samelson, and J. C. Kindle (2006), Dynamics of the California undercurrent in the Navy coastal ocean model, *Eos Trans. AGU*, 87(36), Ocean Sci. Meet. Suppl., Abstract OS-36G–15.

D'Asaro, E. (2004), Lagrangian trajectories on the Oregon shelf during upwelling, *Cont. Shelf Res.*, 24, 1421–1436, doi:10.1016/j.csr.2004.06.003.

Dale, A. C., and J. A. Barth (2001), The hydraulics of an evolving upwelling jet flowing around a cape, *J. Phys. Oceanogr.*, 31, 226–243, doi:10.1175/1520-0485(2001)031<0226:THOAEU>2.0.CO;2.

Dever, E. (1997), Wind-forced cross-shelf circulation on the northern California shelf, *J. Phys. Oceanogr.*, 27, 1566–1580, doi:10.1175/1520-0485(1997)027<1566:WFCSCO>2.0.CO;2.

Dinniman, M. S., and J. M. Klinck (2002), The influence of open versus periodic alongshore boundaries on circulation near submarine canyons, *J. Atmos. Oceanic Technol.*, 19, 1722–1737, doi:10.1175/1520-0426(2002)019<1722:TIOOVP>2.0.CO;2.

Durski, S. M., and J. S. Allen (2005), Finite-amplitude evolution of instabilities associated with the coastal upwelling front, *J. Phys. Oceanogr.*, 35, 1606–1628, doi:10.1175/JPO2762.1.

Fairall, C. W., E. F. Bradley, D. P. Rogers, J. B. Edson, and G. S. Young (1996), Bulk parameterization of air-sea fluxes for Tropical Ocean-Global Atmosphere Coupled-Ocean Atmosphere Response Experiment, *J. Geophys. Res.*, 101, 3747–3764, doi:10.1029/95JC03205.

Flather, R. A. (1976), A tidal model of the north-west European continental shelf, *Mem. Soc. R. Sci. Liège 6 Sér.*, 10, 141–164.

Gan, J., and J. S. Allen (2005a), Modeling upwelling circulation off the Oregon coast, *J. Geophys. Res.*, 110, C10S07, doi:10.1029/2004JC002692.

Gan, J. P., and J. S. Allen (2005b), On open boundary conditions for a limited-area coastal model off Oregon. Part 1: Response to idealized wind forcing, *Ocean Modell.*, 8, 115–133, doi:10.1016/j.ocemod.2003.12.006.

Gan, J. P., J. S. Allen, and R. M. Samelson (2005), On open boundary conditions for a limited-area coastal model off Oregon. Part 2: Response to wind forcing from regional mesoscale atmospheric model, *Ocean Modell.*, 8, 155–173, doi:10.1016/j.ocemod.2003.12.007.

Haidvogel, D. B., et al. (2008), Ocean forecasting in terrain-following coordinates: Formulation and skill assessment of the Regional Ocean Modeling System, *J. Comput. Phys.*, 227, 3595–3624, doi:10.1016/j.jcp.2007.06.016.

Halliwell, G. R., Jr., and J. S. Allen (1984), Large-scale sea level response to atmospheric forcing along the west coast of North America, summer 1973, *J. Phys. Oceanogr.*, 14, 864–886, doi:10.1175/1520-0485(1984)014<0864:LSSLRT>2.0.CO;2.

Hodur, R. M. (1997), The Naval Research Laboratory's Coupled Ocean/Atmosphere Mesoscale Prediction System (COAMPS), *Mon. Weather Rev.*, 125, 1414–1430, doi:10.1175/1520-0493(1997)125<1414:TNRLSC>2.0.CO;2.

Huyer, A. (1983), Coastal upwelling in the California Current System, *Prog. Oceanogr.*, 12, 259–284, doi:10.1016/0079-6611(83)90010-1.

Huyer, A., P. A. Wheeler, P. T. Strub, R. L. Smith, R. Letelier, and P. M. Kosro (2007), The Newport line off Oregon–Studies in the north east Pacific, *Prog. Oceanogr.*, 75, 126–160, doi:10.1016/j.pocean.2007.08.003.

Kalnay, E., et al. (1996), The NCEP/NCAR 40-Year reanalysis project, *Bull. Am. Meteorol. Soc.*, 77, 437–471, doi:10.1175/1520-0477(1996)077<0437:TNYRP>2.0.CO;2.

Kindle, J. C., R. M. Hodur, S. deRada, J. D. Paduan, L. K. Rosenfeld, and F. Q. Chavez (2002), A COAMPS™ reanalysis for the Eastern Pacific: Properties of the diurnal sea breeze along the central California coast, *Geophys. Res. Lett.*, 29(24), 2203, doi:10.1029/2002GL015566.

Kosro, P. M. (2005), On the spatial structure of coastal circulation off Newport, Oregon, during spring and summer 2001 in a region of varying shelf width, *J. Geophys. Res.*, 110, C10S06, doi:10.1029/2004JC002769.

Kuebel Cervantes, B. T., and J. S. Allen (2006), Numerical model simulations of shelf flows off northern California, *Deep Sea Res., Part II*, 53, 2956–2984, doi:10.1016/j.dsr2.2006.07.004.

Kuebel Cervantes, B. T., J. S. Allen, and R. M. Samelson (2003), A modeling study of Eulerian and Lagrangian aspects of shelf circulation off Duck, North Carolina, *J. Phys. Oceanogr.*, 33, 2070–2092, doi:10.1175/1520-0485(2003)033<2070:AMSOEA>2.0.CO;2.

Kundu, P. K. (1976), Ekman veering observed near the ocean bottom, *J. Phys. Oceanogr.*, 6, 238–242, doi:10.1175/1520-0485(1976)006<0238:EVONTO>2.0.CO;2.

Kurapov, A. K., J. S. Allen, G. D. Egbert, and R. N. Miller (2005a), Modeling bottom mixed layer variability on the mid-Oregon shelf during summer upwelling, *J. Phys. Oceanogr.*, 35, 1629–1649, doi:10.1175/JPO2768.1.

Kurapov, A. K., J. S. Allen, G. D. Egbert, R. N. Miller, P. M. Kosro, M. Levine, and T. Boyd (2005b), Distant effects of assimilation of moored currents into a model of coastal wind-drive circulation off Oregon, *J. Geophys. Res.*, 110, C02022, doi:10.1029/2003JC002195.

Kurapov, A. K., J. S. Allen, G. D. Egbert, R. N. Miller, P. M. Kosro, M. Levine, and T. Boyd (2005c), Assimilation of moored velocity data into a model of coastal wind-drive circulation off Oregon: Multivariate capabilities, *J. Geophys. Res.*, 110, C10S08, doi:10.1029/2004JC002493.

Marchesiello, P., J. C. McWilliams, and A. Shchepetkin (2001), Open boundary conditions for long-term integrations of regional oceanic models, *Ocean Modell.*, 3, 1–20, doi:10.1016/S1463-5003(00)00013-5.

Marchesiello, P., J. C. McWilliams, and A. Shchepetkin (2003), Equilibrium Structure and Dynamics of the California Current System, *J. Phys. Oceanogr.*, 33, 753–783, doi:10.1175/1520-0485(2003)33<753:ESADOT>2.0.CO;2.

Mellor, G. L., and T. Yamada (1982), Development of a turbulence closure model for geophysical fluid problems, *Rev. Geophys.*, 20, 851–875, doi:10.1029/RG020i004p00851.

National Geophysical Data Center (1988), Digital relief of the surface of the Earth, *Data Announce. 88-MGG-02*, NOAA, Boulder, Colo.

Oke, P. R., J. S. Allen, R. N. Miller, G. D. Egbert, J. A. Austin, J. A. Barth, T. J. Boyd, P. M. Kosro, and M. D. Levine (2002a), A modeling study of the three-dimensional continental shelf circulation off Oregon. Part I: Model-data Comparisons, *J. Phys. Oceanogr.*, 32, 1360–1382, doi:10.1175/1520-0485(2002)032<1360:AMSOTT>2.0.CO;2.

Oke, P. R., J. S. Allen, R. N. Miller, and G. D. Egbert (2002b), A modeling study of the three-dimensional continental shelf circulation off Oregon. Part II: Dynamical analysis, *J. Phys. Oceanogr.*, 32, 1383–1403, doi:10.1175/1520-0485(2002)032<1383:AMSOTT>2.0.CO;2.

Paulson, C. A., and J. J. Simpson (1977), Irradiance measurements in the upper ocean, *J. Phys. Oceanogr.*, 7, 952–956, doi:10.1175/1520-0485(1977)007<0952:IMITUO>2.0.CO;2.

Perlin, N., R. M. Samelson, and D. B. Chelton (2004), Scatterometer and model wind and wind stress in the Oregon–Northern California Coastal Zone, *Mon. Weather Rev.*, 132, 2110–2129, doi:10.1175/1520-0493(2004)132<2110:SAMWAW>2.0.CO;2.

Peterson, W. T., and J. E. Keister (2002), The effect of a large cape on distribution patterns of coastal and oceanic copepods off Oregon and northern California during the 1998–1999 El Niño–La Niña, *Prog. Oceanogr.*, 53, 389–411, doi:10.1016/S0079-6611(02)00038-1.

Pierce, S. L., R. L. Smith, P. M. Kosro, J. A. Barth, and C. D. Wilson (2000), Continuity of the poleward undercurrent along the eastern boundary of the mid-latitude north Pacific, *Deep Sea Res., Part II*, 47, 811–829, doi:10.1016/S0967-0645(99)00128-9.

Powell, T. P., C. V. W. Lewis, E. N. Curchitser, D. B. Haidvogel, A. J. Hermann, and E. L. Dobbins (2006), Results from a three-dimensional, nested biological-physical model of the California Current System and comparisons with statistics from satellite imagery, *J. Geophys. Res.*, 111, C07018, doi:10.1029/2004JC002506.

Pullen, J. D., and J. S. Allen (2000), Modeling studies of the coastal circulation off northern California: Shelf response to a major Eel River flood event, *Cont. Shelf Res.*, 20, 2213–2238, doi:10.1016/S0278-4343(00)00068-6.

Rio, M.-H., and F. Hernandez (2004), A mean dynamic topography computed over the world ocean from altimetry, in situ measurements, and a geoid model, *J. Geophys. Res.*, 109, C12032, doi:10.1029/2003JC002226.

Samelson, R., P. Barbour, J. Barth, S. Bielli, T. Boyd, D. Chelton, P. Kosro, M. Levine, E. Skyllingstad, and J. Wilczak (2002), Wind stress forcing of the Oregon coastal ocean during the 1999 upwelling season, *J. Geophys. Res.*, 107(C5), 3034, doi:10.1029/2001JC000900.

Shchepetkin, A. F., and J. C. McWilliams (2003), A method for computing horizontal pressure-gradient force in an oceanic model with a nonaligned vertical coordinate, *J. Geophys. Res.*, 108(C3), 3090, doi:10.1029/2001JC001047.

Shchepetkin, A. F., and J. C. McWilliams (2005), The regional oceanic modeling system (ROMS): A split-explicit, free-surface, topography-following-coordinate oceanic model, *Ocean Modell.*, 9, 347–404, doi:10.1016/j.ocemod.2004.08.002.

Shulman, I., J. C. Kindle, S. deRada, S. C. Anderson, B. Penta, and P. J. Martin (2004), Development of a hierarchy of nested models to study the California current system, in *Estuarine and Coastal Modeling 2003, 8th International Conference on Estuarine and Coastal Modeling*, edited by M. L. Spaulding, Am. Soc. of Civil Eng., Monterey, Calif.

Smith, R. L. (1981), A comparison of the structure and variability of the flow field in three coastal upwelling regimes: Oregon, northwest Africa, and Peru, in *Coastal Upwelling, Coastal and Estuarine Sci.*, vol. 1, edited by F. A. Richards, pp. 107–118, AGU, Washington, D. C.

Song, Y., and D. Haidvogel (1994), A semi-implicit ocean circulation model using a generalized topography-following coordinate system, *J. Comput. Phys.*, 115, 228–244, doi:10.1006/jcph.1994.1189.

Strub, P. T., and C. James (2000), Altimeter-derived variability of surface velocities in the California Current System: 2. Seasonal circulation and eddy statistics, *Deep Sea Res., Part II*, 47, 831–870, doi:10.1016/S0967-0645(99)00129-0.

Wijesekera, H. W., J. S. Allen, and P. A. Newberger (2003), Modeling study of turbulent mixing over the continental shelf: Comparison of turbulent closure schemes, *J. Geophys. Res.*, 108(C3), 3103, doi:10.1029/2001JC001234.

————————————

J. S. Allen, G. D. Egbert, A. L. Kurapov, R. N. Miller, R. M. Samelson, and S. R. Springer, College of Oceanic and Atmospheric Sciences, Oregon State University, Corvallis, OR 97331, USA. (springer@esr.org)

J. C. Kindle, Oceanography Division, Naval Research Laboratory, Stennis Space Center, MS 39529, USA.